A Systematic Study of Positron/Muon Tracks in the J-PARC/E36 Segmented Scintillating Fibre Target

by

Philipp Stephan

A THESIS SUBMITTED IN PARTIAL FULFILLMENT
OF THE REQUIREMENTS FOR THE DEGREE OF

Master of Science

in

THE FACULTY OF SCIENCE
(Physics)

The University of British Columbia
(Vancouver)

April 2018

Abstract

In order to test lepton universality in the Standard Model, a precision measurement of $\Gamma(\mathrm{K}^+ \to \mathrm{e}^+\nu)/\Gamma(\mathrm{K}^+ \to \mu^+\nu)$ has been performed with the J-PARC/E36 experiment. Reliable positron/muon particle identification is crucial for the successful improvement of the current experimental value. This thesis explains the necessary theoretical background of motivation, detector physics, and simulation as well as the detector system of the experiment. The main work is the evaluation and improvement of the efficiency and precision of a tracking procedure in the analysis pipeline. The algorithm in use is described thoroughly and the tools and results of improvements and parameter variations are discussed.

Contents

List of Tables

List of Figures

Acronyms

AC	Aerogel Cherenkov counter.
APD	avalange photodiode.
CSV	Comma Separated Values.
IB	internal bremsstrahlung.
J-PARC	Japan Proton Accelerator Research Complex.
LVF	Lepton Flavor Violation.
MC	Monte Carlo, a stochastic numerical calculation technique.
MPPC	multi-pixel photon counter.
MSSM	Minimal Supersymmetric Standard Model, the minimal SUSY extension of the SM.
MWPC	Multi-Wire Proportional Chamber.
PDF	Portable Document Format.
PGC	(Pb Glass Cherenkov) lead-glass Cherencov counter.
PMT	photomultiplier.
QFT	Quantum Field Theory.
SD	structure dependent processes.
SFT	Spiral Fiber Tracker.
SiPMT	silicon photomultiplier.
SM	Standard Model of particle physics.
SUSY	Super Symmetric Standard Model, a Standard Model expansion.
TOF	time-of-flight.

TREK	Time-Reversal Experiment with Kaons, a research collaboration.
WLS	wave length shifter.

Chapter 1

Introduction

The field of elementary particle physics is concerned with the study of the basic building blocks of the universe and their interactions. To this day, the widely accepted theory of elementary particle physics is the so-called *Standard Model (SM)* (see for example [26]). An overview of the particles in the SM is provided in table 1.1.

Within the SM, matter is composed of particles categorized as *fermions*. They are characterized by their half-integer spin. The fermions themselves can be further divided into *quarks*, which (amongst other interactions) are subject to the *strong force* and *leptons*, which are not. Both families come in three generations, which differ in mass. Each generation includes two quarks or one charged and one neutral lepton. An example of quarks are the up- and down-quarks of the first generation, which form the compound particle "proton". Leptons include the electron and the neutrinos.

The other category of particles are the *bosons*, which carry full-integer spin. These particles, which include the photon, act as force-carriers to mediate the interactions between particles (both fermions and bosons themselves).

This form of the SM has been successfully predicting a broad variety of phenomena to a high degree of accuracy. But, despite its success, there have been a series of observations which stand in contradiction to it. A large amount of mass in the universe is considered *dark matter* and cannot be explained with the SM. This is also true for the problem of *dark energy* [26]. Another common example is the problem of neutrino oscillations [26, 2, 10]. Neutrinos oscillate between their flavours, indicating that they do carry a mass, whereas in the SM they are assumed to be massless [15].

In order to overcome these problems various extensions to the SM have been proposed. The Super Symmetric Standard Model (SUSY) [26] and the Leptoquark theories [25] are some of the most popular ones that try to tackle the difficulties described above. To test and improve these theories and ultimately incorporate the correct formulation into the current model, precision measurements have to be made. At the current level of accuracy of the SM and its competitors, one has to measure predicted quantities very precisely to find deviations which point toward the superior theory.

One assumption of the SM that is challenged by alternative theories is the so-called *lepton universality*. This concept means that the leptons of all three generations/flavours

	Fermions			**Bosons**	
Generation	I	II	III	gauge	scalar
Quarks	u up	c charm	t top	g gluon	H Higgs
	d down	s strange	b bottom	γ photon	
Leptons	e electron	μ muon	τ tau	Z Z boson	
	ν_{e} electron neutrino	ν_μ muon neutrino	ν_τ tau neutrino	W W boson	

Table 1.1: The particles of the SM according to [26].

(again, see table 1.1) couple to the gauge bosons with identical strength. In particular, this is true for their coupling to the *weak force* mediated by W and Z bosons.

The goal of the experiment discussed in this thesis is to test lepton universality to a higher level of accuracy than it has currently been done. A possible test for this universality can be found by studying *kaon* decays. Kaons are *mesons*, compound particles made of a quark and an antiquark. For the kaon, this is either an up or a down type quark and a strange quark. The decay channels of interest to this experiment are the ones resulting in either a positron or antimuon and a corresponding neutrino (see figure 2.1). For reasons discussed in section 2.1.2, the quantity investigated here is the ratio of the positronic over the muonic decay mode. The SM predicts this ratio to be of order 10^{-5} [7][1].

In order to search for deviations of this ratio, several experiments have been conducted to measure it to a very high degree of accuracy. Measurements at KLOE [3] and NA62 [28] both found values consistent with the SM prediction.

The experiment considered in this thesis, called “J-PARC/E36”, tries to supersede the ones mentioned before and aims for an uncertainty on the ratio of 0.25 % [29]. In contrast to the in-flight measurements at KLOE or NA62, a stopped kaon beam is employed. The measurements have already been taken at the Japan Proton Accelerator Research Complex (J-PARC) and need to be analyzed now. Since the ratio of positrons over antimuons is very small, particle identification between these two is crucial for achieving a high level of accuracy. Several methods outlined in section 3.1.4 are combined to guarantee that positrons are identified at the highest possible rate. Having a small number of events in the numerator of the fraction makes it essential to detect all of them to not skew the ratio significantly.

One step in this analysis pipeline is concerned with reconstructing a particle trajectory

---

[1] The exact value is given in equation 2.14.

through a magnetic field after it exits the detector target. For this tracking to be precise the outgoing angle of the particle as it leaves the target needs to be known as accurately as possible. This thesis evaluates and improves the algorithm used to determine this outgoing angle.

Chapter 2

Theory

This chapter gives some theoretical background to terms and quantities related to the experiment.

As it is usual in the field of particle physics ([see for example 27, sec. “Units and Conventions”]), Einstein’s summation convention for paired raised and lowered indices, $x_\alpha y^\alpha = \sum_\alpha x_\alpha y^\alpha$, is used, where greek indices run $0, 1, 2, 3$ and latin indeces $1, 2, 3$.

In the same manner the natural system of units is used, where the speed of light c and the reduced Planck constant $\hbar$ are defined to be $c \equiv \hbar \equiv 1$. Energy in units of eV is chosen as the base dimension. Thus, masses are also measured in units of eV, whereas time and distance are given in eV^{-1}.

2.1 Kaon Decay

2.1.1 Kaons

Kaons are *mesons*, particles consisting of a quark-antiquark pair. Specifically they are made of a strange antiquark and a quark from the first generation, namely up and down; antikaons from their respective antiparticles. An overview over the various kaons and their properties is given in table 2.1.

The K^0 and $\overline{\mathrm{K}}^0$ are the pure quark eigenstates of the strong force. However kaons decay via the weak force, these strong eigenstates mix into the weak eigenstates K^0_S and K^0_L, which are 50 % K^0 and 50 % $\overline{\mathrm{K}}^0$. They are named after their lifetimes, which differ over a couple of orders of magnitude. There is also oscillation between short and long eigenstates, which will not be discussed further.

For the remainder of this thesis, the K^+ will be the particle of interest.

2.1.2 Decay Width

As the goal of the experiment is testing of lepton universality, a quantity needs to be examined, that is theoretically predictable to a high degree of accuracy in the SM and is also measurable in an experiment. *Lepton universality* refers to the equal strength of the

Type	Symbol	Quarks	Mass (MeV)	Lifetime (s)
K meson	K^0	$\mathrm{d}\ \bar{\mathrm{s}}$	497.611	—
	K^+	$\mathrm{u}\ \bar{\mathrm{s}}$	493.677	1.2380×10^{-8}
K antimeson	$\overline{\mathrm{K}}^0$	$\bar{\mathrm{d}}\ \mathrm{s}$	497.611	—
	K^-	$\bar{\mathrm{u}}\ \mathrm{s}$	493.677	1.2380×10^{-8}
K-short	K^0_S	$(\mathrm{d}\bar{\mathrm{s}} + \mathrm{s}\bar{\mathrm{d}})/\sqrt{2}$	—	0.8954×10^{-10}
K-long	K^0_L	$(\mathrm{d}\bar{\mathrm{s}} - \mathrm{s}\bar{\mathrm{d}})/\sqrt{2}$	—	5.116×10^{-8}

Table 2.1: The various kaons according to [26]. The mixed states K-long and K-short are their own antiparticles. K^0 and $\overline{\mathrm{K}}^0$ are strong eigenstates, yet they decay weakly, therefore one has to refer to the mixed states K^0_S and K^0_L for their lifetimes. For these the mass of the K^0 can be assumed, yet there is a known mass difference $m_{\mathrm{K}^0_\mathrm{L}} - m_{\mathrm{K}^0_\mathrm{S}} = (3.484 \pm 0.006) \times 10^{-12}\,\mathrm{MeV}$.

coupling g_ℓ of the weak force among all three generations or *flavors* of leptons

$$g_\mathrm{e} = g_\mu = g_\tau \,. \tag{2.1}$$

The weak force is mediated through the gauge bosons W and Z, so a process involving these should be considered. As it has purely leptonic decay modes, meaning that its constituent quarks decay into leptons via a weak process, the kaon system described in section 2.1.1 is suitable. Its advantage over e.g. the pion system is explained in section 2.1.5.

The simplest case of leptonic decay for the kaon system is the group of $\mathrm{K}_{\ell 2}$ decays.

$$\begin{aligned} \mathrm{K}_{\ell 2}: \quad \mathrm{K}^+ &\to \ell^+ \nu_\ell \,, \\ \mathrm{K}_{\mathrm{e}2}: \quad \mathrm{K}^+ &\to \mathrm{e}^+ \nu_\mathrm{e} \,, \\ \mathrm{K}_{\mu 2}: \quad \mathrm{K}^+ &\to \mu^+ \nu_\mu \,, \end{aligned} \tag{2.2}$$

where a charged kaon decays into an antilepton ℓ^+, namely positron or antimuon, and the corresponding neutrino (not antineutrino). The Feynman graph for these decays is shown in figure 2.1.

Having the mass of the kaon as available energy to produce the leptons, the excess energy is available to them as kinetic energy. The positrons of $\mathrm{K}_{\mathrm{e}2}$ are emitted with a momentum of 247 MeV, the antimuons with 236 MeV [29, fig. 7].

If one wants to describe these kinds of decay processes mathematically, the methodology of Quantum Field Theory (QFT) is to be used. Particles and system states are described as Fock-space state vectors, where $|\alpha\rangle$ is a vector, and $\langle\alpha|$ is the corresponding linear functional in the dual space. Decays can then be described by a so-called *scattering*

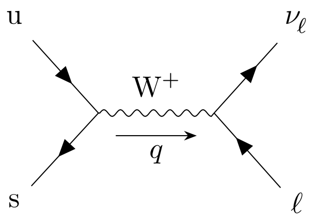

FIGURE 2.1: Feynman graph of the decay $K^+ \to \ell^+ \nu_\ell$ ($K_{\ell 2}$), which is studied to test lepton universality in the SM. Graph generated with [9].

matrix S, which transforms the incoming state $|\text{in}\rangle$ into the outgoing state $|\text{out}\rangle$ like

$$|\text{in}\rangle = S\,|\text{out}\rangle \; . \tag{2.3}$$

The matrix elements are then

$$S_{\text{fi}} = \langle\text{in}|\text{out}\rangle = \langle\text{out}|S|\text{out}\rangle \; , \tag{2.4}$$

where i stands for "initial" and f for "final". As processes with identical initial and final state are not interesting, the scattering matrix is usually split into unity and a *transition matrix* T, which describes real transition processes:

$$S = \mathbb{1} + \mathrm{i}T \, . \tag{2.5}$$

Since processes have to adhere to four-momentum conversation, this is usually also separated. One is left with the *Feynman amplitude* $\mathcal{M}_{\text{fi}}$

$$\mathrm{i}T_{\text{fi}} = \mathrm{i}\mathcal{M}_{\text{fi}} \cdot (2\pi)^4 \delta^4 \left(\sum_{\text{initial}} p_i - \sum_{\text{final}} k_f \right) . \tag{2.6}$$

Here p_i denote the incoming momenta and k_f the outgoing ones. More details on the scattering matrix formalism can be found for example in [27].

The Feynman amplitude is a purely mathematical tool; and, an observable needs to be calculated from it in order to make predictions, which can be tested experimentally. A common observable for decay processes is the *decay width* Γ. The total decay width

$$\Gamma_{\text{tot}} = \frac{\hbar}{\tau} \tag{2.7}$$

can be thought of reciprocal to the lifetime τ of a particle [15]. Here $\hbar \equiv h/(2\pi)$ denotes the reduced Planck constant. Many particles cannot decay in only one way, they can decay into different sets of outgoing particles, called *decay channels*. Every decay channel i has a decay width $\Gamma(i)$, and the total decay width is the sum over the decay widths of all possible decay channels

$$\Gamma_{\text{tot}} = \sum_i \Gamma(i)\,. \tag{2.8}$$

By taking the fraction of a decay width of of an individual decay channel i over the total decay width, one finds the *branching ratio*

$$\mathrm{BR}(i) = \frac{\Gamma(i)}{\Gamma_{\text{tot}}} \tag{2.9}$$

for that decay. The branching ratio gives the probability for a certain decay channel.

For the $\mathrm{K}_{\ell 2}$ decay, the Feynman amplitude is given as [29, eqn. 1]

$$\mathcal{M} = g_\ell \frac{G}{\sqrt{2}} q^\alpha\, f(q^2)\, \left(\bar{u}_\ell \gamma_\alpha (1-\gamma_5) u_\nu\right)\,. \tag{2.10}$$

Here g_ℓ is the weak coupling constant for the lepton flavor ℓ and according to the SM's lepton universality should be equal for electrons and muons ($g_\mathrm{e}/g_\mu = 1$). G is Fermi's coupling constant, $\{\gamma_\alpha\}$, γ_5 are the Dirac matrices, and the $u_{\ell,\nu}$ are the spinors for massive leptons and neutrinos respectively. The momentum transfer during the decay is referred to as q. As kaons are compound particles that have a substructure, it would have to be taken into account. The interaction between the constituent quarks and gluons is the same for all kaon processes at a certain energy, so it can be encapsulated in the *form factor* f. Considering $\mathrm{K}_{\ell 2}$, the momentum transfer is the mass of the kaon $q^2 = m_\mathrm{K}^2$, therefore $f(m_\mathrm{K}^2) =: f_\mathrm{K}$. This yields

$$\mathcal{M} = g_\ell \frac{G}{\sqrt{2}} f_\mathrm{K} m_\ell \bar{u}_\ell (1-\gamma_5) u_\nu\,. \tag{2.11}$$

According to [29, eqn. 3], the observable decay width for the $\mathrm{K}_{\ell 2}$ decay can now be calculated from the amplitude as

$$\Gamma(\mathrm{K}_{\ell 2}) = g_\ell^2 \frac{G^2}{8\pi} f_\mathrm{K}^2 m_\mathrm{K} m_\ell^2 \left(1 - \frac{m_\ell^2}{m_\mathrm{K}^2}\right)^2\,. \tag{2.12}$$

As noted earlier, the f_K is a constant that describes the complex inner workings of the kaon compound system. It is hard to calculate theoretically; hence, it's inclusion in the observable decay width would decrease the precision of the SM prediction. To avoid the issue, the observable predicted by the SM and tested by this experiment is not a single $\mathrm{K}_{\ell 2}$ decay width, but the *ratio* of the positronic over the muonic decay width [29, eqn. 4]

$$\begin{aligned} R_\mathrm{K}^\mathrm{SM} &= \frac{\Gamma(\mathrm{K}_{\mathrm{e}2})}{\Gamma(\mathrm{K}_{\mu 2})} = \frac{\Gamma(\mathrm{K}^+ \to \mathrm{e}^+\nu)}{\Gamma(\mathrm{K}^+ \to \mu^+\nu)} \\ &= \frac{g_\mathrm{e}^2}{g_\mu^2} \frac{m_\mathrm{e}^2}{m_\mu^2} \left(\frac{m_\mathrm{K}^2 - m_\mathrm{e}^2}{m_\mathrm{K}^2 - m_\mu^2}\right)^2 (1 + \delta_\mathrm{r})\,. \end{aligned} \tag{2.13}$$

By taking the ratio, the form factor and Fermi's coupling cancel out, leaving only a dependence on the kaon and lepton masses as well as the ratio of the weak coupling constants for the leptons. The inclusion of the radiative correction δ_r is discussed in section 2.1.3.

The current theoretical prediction for this ratio within the SM is [7, eqn. 16]

$$R_\mathrm{K}^\mathrm{SM} = (2.477 \pm 0.001) \times 10^{-5}\,. \tag{2.14}$$

Since the masses of the respective kaon and leptons are well known [26], comparing the theoretical prediction with the experimental result, $R_\mathrm{K}^\mathrm{exp}$ gives a test for lepton universality

$$g_\mu / g_\mathrm{e} = \sqrt{R_\mathrm{K}^\mathrm{exp} / R_\mathrm{K}^\mathrm{SM}}\,. \tag{2.15}$$

Any deviation of the experimental from the SM ratio implies a deviation of the weak coupling constants over the different lepton flavors [21, sec. 1.1].

The experimental value for the ratio $R_\mathrm{K}^\mathrm{exp}$ is derived from the number of registered positronic $N(\mathrm{K}_{\mathrm{e}2})$ and muonic $N(\mathrm{K}_{\mu 2})$ kaon decays. Again, decays with internal bremsstrahlung as described in section 2.1.3, are included in this count, whereas structure dependent processes are not. These numbers have to be corrected by the detector acceptance rates $\mathit{\Omega}$ to yield the actual value of the ratio [32, eqn. 2.2]

$$R_\mathrm{K}^\mathrm{exp} = \frac{N(\mathrm{K}_{\mathrm{e}2})}{N(\mathrm{K}_{\mu 2})}\,\frac{\mathit{\Omega}(\mathrm{K}_{\mu 2})}{\mathit{\Omega}(\mathrm{K}_{\mathrm{e}2})}\,. \tag{2.16}$$

It helps reducing the overall systematic uncertainties that the value depends only on the *ratio* of the detector acceptances. The total uncertainty of $R_\mathrm{K}^\mathrm{exp}$ obtained from this experiment is expected to be 0.25 % [32, sec. 2.1].

2.1.3 Radiative Corrections

Bremsstrahlung refers to the emission of electromagnetic radiation by a charged particle that is accelerated in an external electro-magnetic field. In the context of QFT, this is the emission of additional photons in the final state [27, chap. 6].

In processes involving compound meson particles, which are described with an effective theory using form factors[1], emissions of photons are divided into two categories [24, caption fig. 1, 4, sec. 1]. This is illustrated by the Feynman graphs in figure 2.2.

Internal bremsstrahlung (IB) refers to the emission of a photon from vertices corresponding to the meson, leptons or the gauge boson (figures 2.2a to 2.2c). In contrast, structure dependent processes (SD) involve the emission from the parts hidden away by the effective theory (figures 2.2d and 2.2e).

In the theoretical calculations of the ratio R_K^SM, the IB corrections are included, but SD are not [29, sec. 1.1, 7, sec. "Results"]. This gives a value for the correction of

---

[1] See discussion in section 2.1.2

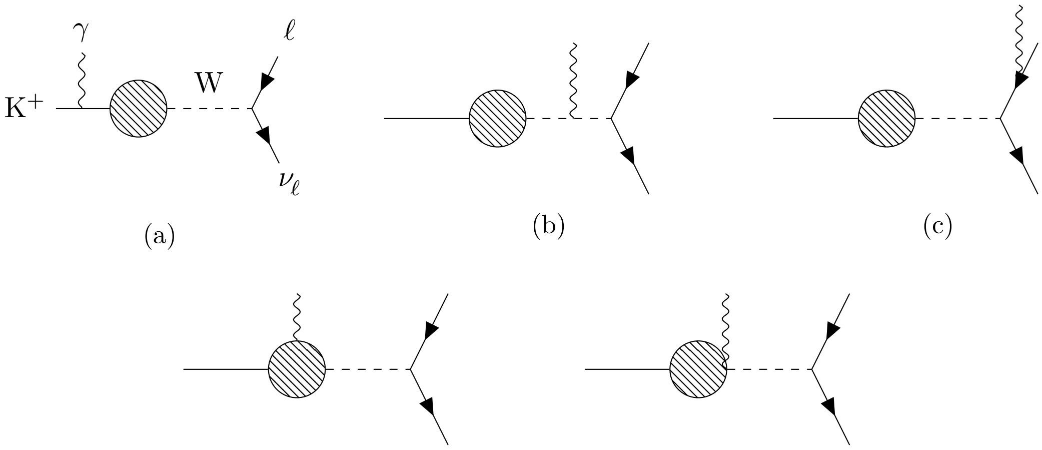

(a) (b) (c)

(d) (e)

FIGURE 2.2: The different radiative processes occurring during a $\mathrm{K}_{\ell 2}$ decay. The circular blob represents internal processes of the meson which are encapsulated by the effective theory. Figures 2.2a to 2.2c are categorized as internal bremsstrahlung, figures 2.2d and 2.2e as structure dependent processes. Figure adapted from [24, fig. 1] and graphs generated with [9].

$\delta_\mathrm{r} = -0.036$ [7]. Explicitly, $\mathrm{K}^+ \to \mathrm{e}^+\nu_\mathrm{e}\gamma$ ($\mathrm{K}^\mathrm{IB}_{\mathrm{e}2\gamma}$) and $\mathrm{K}^+ \to \mu^+\nu_\mu\gamma$ ($\mathrm{K}^\mathrm{IB}_{\mu 2\gamma}$) are included [19].

2.1.4 Helicity Suppression

The cause of the big difference of the branching ratios of the electronic and muonic channels can be explained by the concept of *helicity suppression* [16, sec. 12.6]

Chirality is the behavior of the group theoretical description of a particle under parity transformation. Particles that transform under the chirality operator $\gamma^5 = \mathrm{i}\gamma^0\gamma^1\gamma^2\gamma^3$, γ^μ being the Dirac matrices, with a positive eigenvalue are called *right-handed*, those with a negative one *left-handed*.

Helicity is the projection of a particle's spin onto the direction of its momentum. Spin and momentum pointing in the same direction is denoted as *right-handed*, them being opposite as *left-handed*.

For massless particles, one can not boost into a frame of reference where direction of momentum is reversed, so chirality and helicity are identical. For massive particles on the other hand, this is always possible, making helicity frame dependent.

A peculiarity of the weak interaction is, that it only couples to particles of left-handed chirality (and right-handed antiparticles). This can be seen in equation 2.10, where $(1 - \gamma_5)/2$ denotes a projection of the neutrino spinor into the left-handed state.

Considering the decay in the rest frame of the kaon, its momentum is zero. As momentum is conserved, the final state also has to have a vanishing net momentum. Same is true for the net spin, the kaon having $s = 0$.

Neutrinos are assumed to be massless in the SM; hence, for the $\mathrm{K}_{\ell 2}$ decay the chirality, as well as the helicty of the final state neutrino, has to be left-handed. Thus, its spin is opposite to its direction of momentum. Enforcing momentum and spin conservation, the antilepton has to be emitted with a momentum in the opposite direction of the neutrino. Its spin also has to be pointing to the opposite direction as the neutrino's spin. Hence, its helicity has to be left-handed as well.

But, being an *anti*particle its chirality has to be *right*-handed to couple to the W-boson. If the antilepton were massless as well, this decay would therefore be completely forbidden. Yet, since it does carry a mass, chirality and helicity are not identical. While acquiring a mass through the Higgs mechanism, the chirality states are mixed. The antilepton is produced by the weak interaction in a pure right-handed chirality state, but its mass lets it evolve into a mixture of left- and right-handed chirality [5]. In the end, the helicity requirement enforces the left-handed chirality final state.

So, the coupling strength of the chirality mixing is the particles mass. As the positron is a lot lighter ($m_\mathrm{e} \approx 0.5\,\mathrm{MeV}$) compared to the antimuon ($m_\mu \approx 105.7\,\mathrm{MeV}$) [26], its decay channel is heavily suppressed.

2.1.5 Contributions from Other Models

Without going further into details, the contributions made by the Minimal Supersymmetric Standard Model (MSSM) to R_K shall be mentioned. Taking Lepton Flavor Violation (LVF) processes included in this model into consideration, the deviation from the SM prediction can be written as

$$R_\mathrm{K}^\mathrm{LVF} = R_\mathrm{K}^\mathrm{SM} \left(1 + \Delta^\mathrm{LVF}\right) . \tag{2.17}$$

This contribution can be shown [13, eqn. 19] to be proportional to the ratio of the τ over e^- mass, i.e., $\Delta^\mathrm{LVF} \propto m_\tau^2/m_\mathrm{e}^2$. Due to this strong enhancement by τ emission, a contribution at percent level can be reached [21, 29]:

$$R_\mathrm{K}^\mathrm{LVF} = 1.014 \cdot R_\mathrm{K}^\mathrm{SM} \tag{2.18}$$

The LVF process mediated by a charged Higgs in the MSSM is shown in figure 2.3 without further explanation on the involved SUSY particles.

Also being proportional to the involved meson mass, $\Delta^\mathrm{LVF} \propto m_\mathrm{K}^4$ [13, eqn. 19], the LVF contribution shows the superiority of the kaon channel compared to testing lepton universality in the pion channel. The measurement of the same ratio $R_\pi = \Gamma(\pi^+ \to \mathrm{e}^+\nu_\mathrm{e})/\Gamma(\pi^+ \to \mu^+\nu_\mu)$ would not be sensitive to this MSSM contribution, as it is suppressed by a factor of $m_\pi^4/m_\mathrm{K}^4 \approx 0.006$ [29].

2.2 Scintillators

This section follows the discussion in [20, chap. 7].

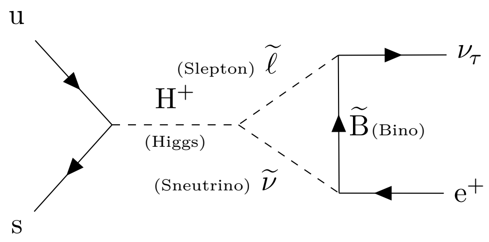

FIGURE 2.3: Feynman graph of a process contributing to R_K, which involves supersymmetric particles and is not possible within the SM. Taken from [29], but graph generated with [9].

A *scintillator* is a material, which emits a flash of light when hit by a particle or radiation. Electrons in the matter are excited into a higher energy state by incident radiation and emit light when relaxing to the ground state. When used as a detector, this light is collected and transformed into a current by a photomultiplier (PMT), which is amplified and finally read by electronics.

Scintillators feature a linear response to the energy deposited in the material as well as a fast response time. This makes them suitable for energy spectroscopy and the collection precise timing information of particle hits. The short recovery time they need after a hit, before they are able to detect another one, allows for high incident particle rates.

Light emission, *luminescence*, is categorized into two classes: *Fluorescence* describes processes where the light emission occurs within 10^{-8} s of radiation absorption. Being of the same order as the transition time an electron takes to change into a different energy state, this emission is regarded as immediate. On the other hand, *phosphorescence* is used to describe delayed emission. The excited state of the electron is metastable, so that the relaxation into the ground state accompanied by photon emission does not happen immediately. The time scale is material specific and can range from microseconds to hours.

Specifically designed materials can include fast and slow transitions, so that their behavior can be described by

$$N(t) = A \cdot \exp\left(-\frac{t}{\tau_\mathrm{f}}\right) + B \cdot \exp\left(-\frac{t}{\tau_\mathrm{s}}\right) . \tag{2.19}$$

Here N describes the number of photons emitted at time t after absorption and τ_f and τ_s are the fast and slow decay constants. The proportion of the respective processes A and B is material specific as well.

As they are the type used in this experiment, this discussion will focus on *organic* scintillators. These are especially well suited for the timing needs of this setup, as they feature rapid decay times in the order of nanoseconds.

The electrons being excited during the scintillation process are the delocalized valence electrons of the aromatic benzene ring structures of the organic material. Occupying the

π-orbitals of the benzene molecules, they are not associated with any one atom, but are delocalized. Because of that, each excited electron singlet and triplet state has a fine structure corresponding to the vibrational modes of the molecule. The electronic energy levels are of the order of a few eV, whereas the vibrational levels are a few tenths of that.

From the first singlet excitation state, the radiative decay mostly relaxes to one of the ground state vibration modes. Therefore, the energy of the emitted photons is smaller than the excitation energy for the first level and the material is transparent to its own emission radiation.

The most widely used form of organic scintillators are plastics. Their major advantage is their mechanical flexibility and ease of production and handling. A good description of their emission behavior is the convolution of a Gaussian with the exponential decay form.

$$N(t) = N_0 f(\sigma, t) \exp\left(-\frac{t}{\tau}\right) , \tag{2.20}$$

where $f(\sigma, t)$ is a Gaussian with a standard deviation of σ. N_0 being the total number of photons emitted and τ the material specific decay constant. For some materials, the more general form of equation 2.19 would have to be adapted.

2.3 Monte Carlo Simulations

In order to understand the detector system better and evaluate systematic errors in the analysis of the events, simulations of decays within the fully modeled detector are performed [29]. These deliver information about the uncertainty of the detector acceptance ratio and inefficiencies of individual parts of the detector system. It also gives insights into the errors introduced by the subtraction of the backgrounds, namely the radiative structure dependent processes (SD) and from pion events.

The evaluation of the analysis algorithm presented in this thesis depends on simulation data as well. As all the data about particle trajectories and energies is known to the simulation, the study of simulated events makes it possible to compare the results of the analysis with the actual values. On experimental data, it is hard to evaluate the correctness of an analysis.

The simulations related to the target analysis in this thesis was performed using the GEANT4 [1] toolkit. It is a software package for *Monte Carlo (MC)* simulations. For more information about the MC methods deployed there, refer to [11, chap. 2].

Monte Carlo methods are a class of numerical calculation algorithms which utilize probabilistic modeling to solve deterministic problems. The brief overview provided here and more in-depth information can be found in [34].

To illustrate how stochastic methods can be used for numerical calculations, the example case of numerical integration will be examined. MC methods are well suited for higher dimensional numerical integration.

Consider the integral

$$I = \int_{\Omega} \mathrm{d}x\, f(x) \tag{2.21}$$

over a domain $\varOmega$. The Monte Carlo estimate for I is then given by

$$E = \frac{1}{N} \sum_{n=1}^{N} f(x_n) \,, \tag{2.22}$$

where $x_n \in \varOmega$ are N random numbers drawn uniformly from the domain of the integral. For $N \to \infty$, the estimate converges to the value of the integral $E \to I$.

2.4 Particle-Detector Interactions

The following interactions between the particles involved in the decay and the detector matter have been considered in the MC simulation.

2.4.1 Delta Production

Delta-rays, δ-rays, or *knock-on electrons*, are electrons ejected from an atom during an ionization process. In this case, it refers to electrons that are "knocked out" off the detector matter by the primary decay product rays. The processes involved in this knock-on electron production is being differentiated for positrons and antimuons; but, it generally involves energy transfer from the decay lepton to a bound electron via collision.

During the MC simulation, the differential cross sections at energy E for collision with an atom of number Z are integrated from a cut-off energy T_{cut} up to a maximum energy $T_{\max}$ to obtain the cross section [11, eqn. 7.2]

$$\sigma(Z, E, T_{\text{cut}}) = \int_{T_{\text{cut}}}^{T_{\max}} \mathrm{d}T \, \frac{\mathrm{d}\sigma(Z, E, T)}{\mathrm{d}T} \,. \tag{2.23}$$

Here, the cutoff energy is always larger than 1 keV.

For positrons, the elementary process considered in the simulation is *Bhabha scattering* $\mathrm{e}^+\mathrm{e}^- \to \mathrm{e}^+\mathrm{e}^-$. These calculations are carried out in the limit of the delta ray energies being much larger than the ionization energy of the detector material ($T \gg I$). The differential cross section is [11, sec. 10.1.4]

$$\frac{\mathrm{d}\sigma}{\mathrm{d}\varepsilon} = \frac{2\pi r_{\mathrm{e}}^2 Z}{\gamma - 1} \left(\frac{1}{\beta^2 \varepsilon^2} - \frac{B_1}{\varepsilon} + B_2 - B_3 \varepsilon + B_4 \varepsilon^2 \right) \,, \tag{2.24}$$

where for the incident positron with mass m and energy E

$$\begin{aligned} \gamma &= E/(mc^2) \text{ (SI units)} \,, & B_1 &= 2 - y^2 \,, \\ \beta^2 &= 1 - (1/\gamma^2) \,, & B_2 &= (1 - 2y)(3 + y^2) \,, \\ y &= 1/(\gamma + 1) \,, & B_3 &= (1 - 2y)^2 + (1 - 2y)^3 \,, \\ \varepsilon &= T/(E - mc^2) \text{ (SI units)} \,, & B_4 &= (1 - 2y)^3 \,. \end{aligned} \tag{2.25}$$

Z is the atomic number for the atom being ionized and $r_{\mathrm{e}} = e^2/(4\pi\varepsilon_0 m_{\mathrm{e}} c^2)$ the classical electron radius [26, tab. 1.1]. Simulations yielded[2] a large amount (23 %) of events with positron delta rays at cutoff $T_{\mathrm{cut}} = 1.25\,\mathrm{MeV}$. A higher cutoff at 25 MeV still yields 7.5 ‰ of events that are affected.

Antimuons produce deltas by *Mott scattering*. In the center-of-mass system, the corresponding cross section is[2] (compare [27, prob. 5.1, p. 169] and [26, sec. 33.2.7])

$$\frac{\mathrm{d}\sigma}{\mathrm{d}\Omega} = \frac{Z^2 e^4 \left(1 - \beta^2 \sin^2 \frac{\theta}{2}\right)}{64\pi^2 \varepsilon_0 c^2 \left|\vec{P}\right|^2 \beta^2 \sin^4 \frac{\theta}{2}} . \tag{2.26}$$

Here e is the elementary charge, ε_0 the dielectric constant, $\vec{P}$ the incident muon three-momentum and SI units are used. The previous definitions also apply.

For a single collision like this, the maximum knock-on electron energy is given by [26, sec. 33.2.2] as

$$T_{\mathrm{max}} = \frac{2 m_{\mathrm{e}} c^2 \beta^2 \gamma^2}{1 + 2\gamma m_{\mathrm{e}}/M + (m_{\mathrm{e}}/M)^2} , \tag{2.27}$$

where M is taken to be the muon mass and the result is in SI units. This yields[2] $T_{\mathrm{max}} = 5.46\,\mathrm{MeV}$ as a maximum delta energy for muon collisions.

In the simulations, the production rate was found[2] to be 31.5 % for a cutoff at $T_{\mathrm{cut}} = 1\,\mathrm{MeV}$, 2.4 % at 4 MeV cutoff.

2.4.2 Annihilation

Being a particle-antiparticle pair, the positron for a $\mathrm{K}_{\mathrm{e}2}$ decay can annihilate with an electron from the atoms of the detector matter as it passes through via

$$\mathrm{e}^- \mathrm{e}^+ \to \gamma\gamma . \tag{2.28}$$

According to the GEANT4 manual [11, sec. 10.3], the cross section used to model this process is

$$\sigma(Z, E) = \frac{Z\pi r_{\mathrm{e}}^2}{\gamma + 1} \left(\frac{\gamma^2 + 4\gamma + 1}{\gamma^2 - 1} \ln\left(\gamma + \sqrt{\gamma^2 - 1}\right) - \frac{\gamma + 3}{\sqrt{\gamma^2 - 1}} \right) , \tag{2.29}$$

where E is the incident positron energy, $\gamma = E/(m_{\mathrm{e}} c^2)$ its Lorentz factor (SI not natural units) and $r_{\mathrm{e}} = e^2/(4\pi\varepsilon_0 m_{\mathrm{e}} c^2)$ the classical electron radius [26, tab. 1.1].

Simulations showed[3] that at positron energies between 203.9 MeV to 255.0 MeV, this process occurred in 3.2 ‰ to 2.6 ‰ of events.

---

[2] J. Imazato, internal document "Consideration of target interaction (1)"

[3] J. Imazato, internal document "Consideration of target interaction (3)"

2.4.3 Bremsstrahlung

As noted in section 2.1.3, charged particles emit photons as they are accelerated in a magnetic field. In this case, the leptons are being decelerated due to the deflection by the atomic nuclei and orbital electrons of the detector matter.

The model implemented for electrons [11, sec. 10.2.1] in GEANT4 is based on the Seltzer-Berger bremstrahlung tables [30]. For this model, the differential cross section with respect to the photon energy k is given by

$$\frac{\mathrm{d}\sigma}{\mathrm{d}k} = \frac{\mathrm{d}\sigma_n}{\mathrm{d}k} + Z\frac{\mathrm{d}\sigma_\mathrm{e}}{\mathrm{d}k}\,, \tag{2.30}$$

where $\mathrm{d}\sigma_n/\mathrm{d}k$ is the differential cross section for interaction with the screened nucleus and $Z\,\mathrm{d}\sigma_\mathrm{e}/\mathrm{d}k$ the one for the orbital electrons for atoms of atomic number Z. Both cross sections are tabulated in [30].

Using these tables in the simulation[4], the energy loss in the detector is estimated to be $5.29\,\mathrm{MeV\,cm^{-1}}$.

---

[4] J. Imazato, internal document “Consideration of target interaction (2)”

Chapter 3

Detector System

The E36 experiment discussed in this thesis has been performed at J-PARC's Hadron Experimental Facility in Ibaraki, Japan by the Time-Reversal Experiment with Kaons (TREK) collaboration. The data was collected between October and December 2015 and it is now being analyzed.

3.1 Overview

An overview of the detector system is provided in figure 3.1. The following discussion summarizes the descriptions given in [29, 21, 19, 33].

3.1.1 Beam, target and SFT

A K^+ beam with a momentum of 780 MeV/c is stopped inside the centered segmented scintillating fiber target of the apparatus, after being slowed down by a BeO degrader. In order to only trigger the analysis on kaon events, a Fitch-type differential Cherenkov counter is placed in front of the target. Its refractive index $n = 1.49$ was chosen so that light is only emitted at the rear surface if kaons in range of 740 MeV to 800 MeV entered it. This setup triggers at more than 99 % K^+ efficiency and misidentifies π^+ as K^+ less than 1 %.

The target is made of scintillating fibers and used to determine the location of the stopping point of the kaon in the transverse plane; more details on the target are provided in section 3.2.

A Spiral Fiber Tracker (SFT) detector is used in order to determine the stopping position along the beam axis. Over the length of 200 mm two double-layer fiber ribbons are wrapped around the target in opposite winding directions. That way the intersection of both signals yields the z-coordinate of the stopping point. Together with the target and tracking information in the magnet, a complete three-dimensional stopping vertex can be calculated.

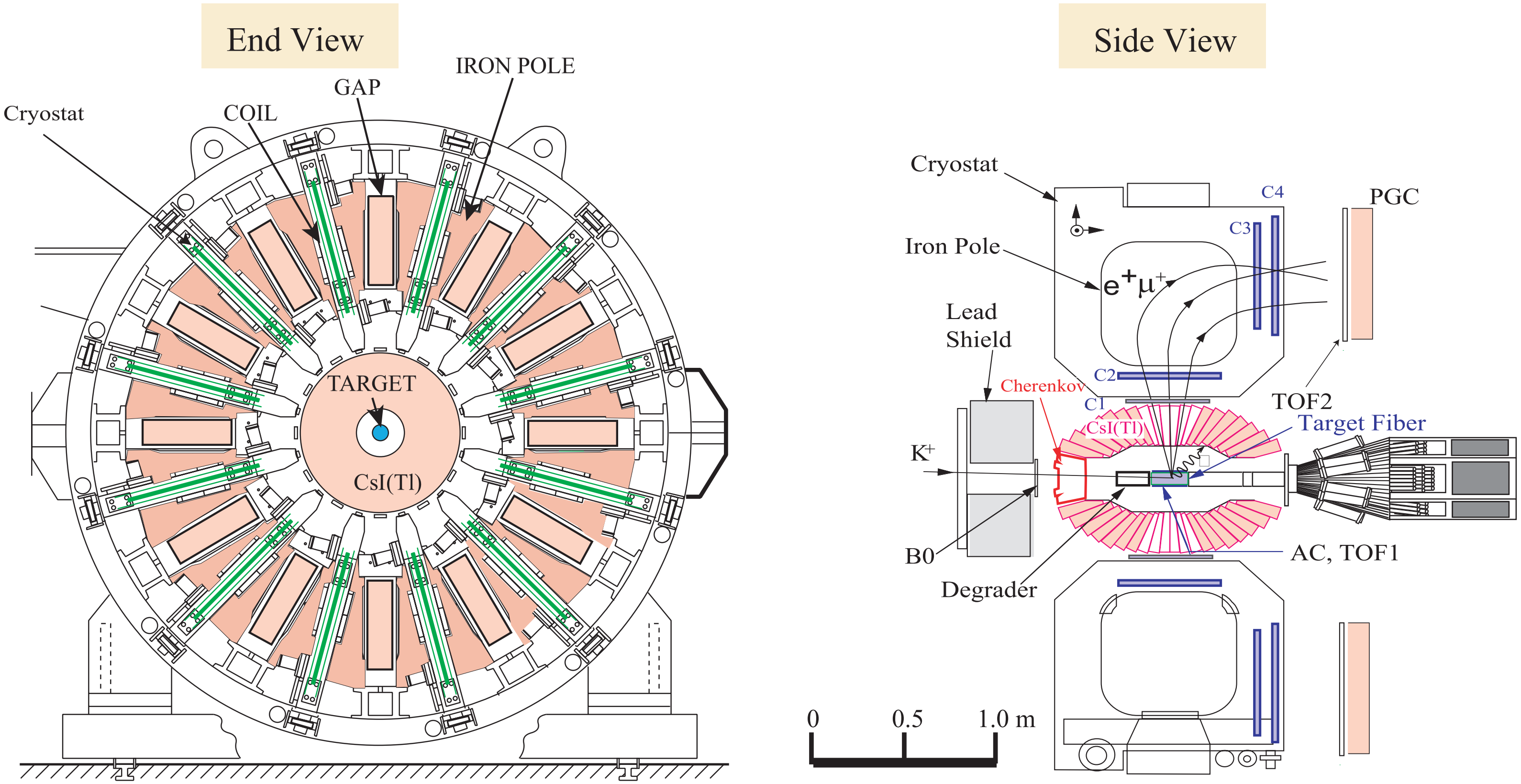

Figure 3.1: The J-PARC/E36 detector system that was used to collect the kaon decay data in end (left) and side (right) view. The target consists of 256 scintillating fibers and is enclosed in a CsI(Tl) calorimeter. Positron/muon discrimination is carried out using the TOF1 and TOF2 counters, the Cherenkov counter, and the lead-glass Cherenkov counter (PGC) (seen in side view). The flight-direction coordinate is measured with a Spiral Fiber Tracker (SFT), consisting of two helices of scintillating fiber with opposite helicity. Figure from [29, fig. 6].

3.1.2 Calorimeter

In order to determine and discard background events that are structure dependent , a photon calorimeter is included in the detector system. Surrounding the target, 768 CsI(Tl) crystals cover 75 % of the solid angle, but leaving gaps for the spectrometer structure described in section 3.1.3 and two holes for beam pass-through. These crystals measure the photon energy for each decay event.

3.1.3 Spectrometer

The core target and calorimeter is surrounded by a superconducting toroidal magnet consisting of twelve iron poles separated by twelve 20 cm gaps (as seen in figure 3.1, end view), in which the magnetic field is generated. Perpendicular to the beam line, the diameter of the detector is about 3 m. To maintain superconductivity, these magnets have to be cooled by a cryostat using liquid helium. During the production runs, these magnets generated a field of 1.4 T. Being exposed to this magnetic field, the trajectories of charged particles[1] emitted from the target are bent 90°. This is used to analyze their momentum as will be discussed below. The particles are tracked by Multi-Wire Proportional Chambers (MWPCs) at the entrance (C2) and exit (C3 and C4) of the magnets.

3.1.4 Particle identification

Particle identification is crucial for a precise measurement of the $R_{\mathrm{K}}^{\mathrm{SM}}$ ratio. As the difference between the $\mathrm{K}_{\mathrm{e}2}$ and $\mathrm{K}_{\mu 2}$ branching ratios spans several orders of magnitude, $\mathrm{K}_{\mathrm{e}2}$, in particular, has to be identified to the highest degree possible. $\mathrm{K}_{\mu 2}$ contamination has to be removed. To achieve this, a redundant system of several detectors is used.

Cherenkov counter AC

A threshold Aerogel Cherenkov counter (AC) is installed around the target. In order to detect positrons (e^+), a refractive index of 1.08 was chosen for the 4.0 cm thick detector. Its efficiency in detecting e^+ is estimated to be greater than 98 % while it's mis-identification rate is 3 %.

TOF measurement

In the low energy region, a time-of-flight (TOF) measurement is performed between 12 pairs of scintillation counters. TOF1 counters are mounted surrounding the target and TOF2 90 cm behind the MWPC C4. Both counters use “BC404” as scintillator material and they are 5 mm and 20 mm thick. BC404 is a plastic scintillator material based on polyvinyltoluene

Typically, the path length of the particle trajectory between TOF1 and TOF2 is around 250 cm. Over this distance, the difference in time-of-flight (TOF) for positrons

---

[1] Muons and positrons from the kaon decays

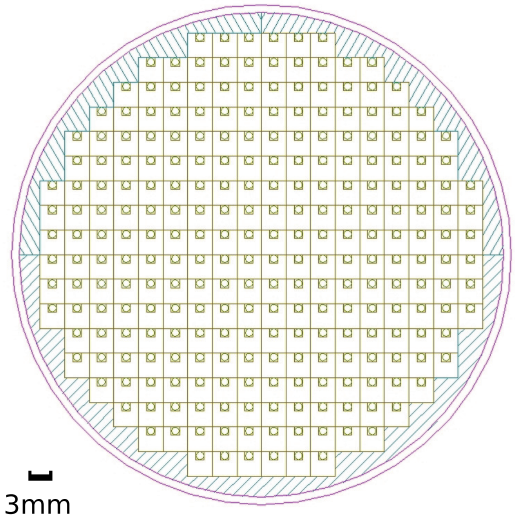

Figure 3.2: Schematic view of the fiber target. Scintillating fibers are represented by green squares, the circular embeddings are the wave length shifters (WLSs). Acrylic binding in blue Figure from [33, fig. 22].

and muons is around 500 ps. With a time resolution of 200 ps, the employed TOF-system is able to differentiate between these particles with an accuracy of 99.993 %.

Lead glass counter PGC

At the end of each magnet gap, 12 cm thick lead-glass Cherenkov counters (PGCs) shower incoming particles. These are also Cherenkov detectors that measure the energy deposit and identify e^+ with an efficiency of 98.5 %.

Mis-idientification Rate

Overall, the muon mis-identification rate is the product of the rates of the individual detectors [compare 23, sec. 3]

$$0.02\ (\mathrm{AC}) \cdot 7 \times 10^{-5}\ (\mathrm{TOF}) \cdot 0.015\ (\mathrm{PGC}) \approx 3 \times 10^{-8}\,. \tag{3.1}$$

3.2 Target

The main target detector, on whose data most of the analysis in this thesis is built upon, is a bundle of scintillating fibers. A schematic of the bundles structure is depicted in figure 3.2.

There are 265 square fibers with a dimension of $(3 \times 3 \times 200)\,\mathrm{mm}^3$ each. As the

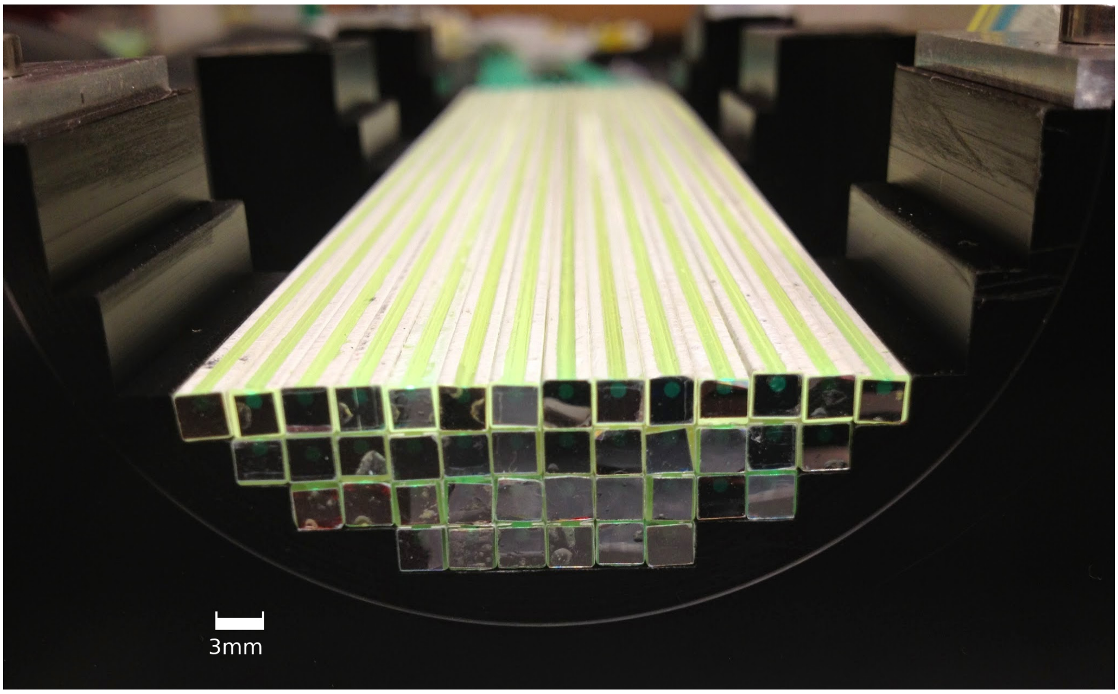

FIGURE 3.3: Photo of the partially assembled fiber target. The green WLS fibers inset in the scintillating fibers are clearly visible along the length of the bundle. Their round cross section can be seen inside the cross section of the square fibers. Picture by J. Imazato.

scintillator material, "BCF-12"[2] by SAINT-GOBAIN was used. To keep the light in the individual fibers, they have been covered with a TiO_2 reflective paint on all sides. This coating is about 40 µm to 50 µm thick, resulting in a total fiber width of around 3.15 mm[3]. The whole bundle is arranged in a circular manner with a diameter of roughly 58 mm. To hold the target together, it is embedded in two stepped acrylic rings and embraced by an aluminum pipe at the downstream end [33, fig. 22]. Together with coating, the fiber bundle spans a total diameter of 65 mm [31, sl. 13].

In each fiber a 1 mm diameter wave length shifter (WLS) is embedded in a 1.1 mm wide and 1.3 mm deep groove carved into the fiber[3]. The WLS fibers guide the light emitted by the scintillator out of the target and into the readout mechanism and shifts its wavelength into the green spectrum. Their total length is about 1.40 m. For the WLS, the S-type "Y-11 (250 ppm)" fiber with double cladding by KURARAY[4] has been used.

The inset fibers are visible in the partially assembled target in figure 3.3.

For analyzing the WLS output, a multi-pixel photon counter (MPPC) by HAMAMATSU

---

[2] For more information, refer to the website of the manufacturer https://www.crystals.saint-gobain.com/products/scintillating-fiber (retrieved 2018-04-16)

[3] M. Hasinoff, private communication

[4] For more information, refer to the manufacturers website at http://kuraraypsf.jp/psf/ws.html (retrieved 2018-04-16)

PHOTONICS[5] is deployed. An MPPC is a silicon photomultiplier (SiPMT) which converts a light signal into an electric current for processing in an electronic analysis pipeline. The functional principle of an MPPC is described in [22].

When a photon hits the detector made of silicon photodiodes with an energy higher than the bandgap of the semiconductor, an electron of the detector material is excited into the conduction band. There a current can flow and is measured by a supporting circuit.

In order to maximize the sensitivity and detect single photons, an avalange photodiode (APD) is used. In a certain region within this APD, a high electric field strength is employed. This accelerates the single excited electron to a high speed, enabling it to ionize detector matter by bumping into another electron. Both electrons are again accelerated and knock off another pair of electrons. This avalanche results in a gain of signal strength by a factor in the range of ten to a few hundred.

To further increase the gain, the APD can be operated in Geiger mode. Increasing the voltage applied to the semiconductor for the avalanche region will eventually transform it into a conductor. This breakdown of semiconductiveness, also known as *Geiger discharge*, is initiated by the first electron entering the avalanche region as the APD can be a stable semiconductor even above the threshold voltage. As the detector becomes a conductor, the current flow increases dramatically, and the signal gain is around 10^5.

The MPPC reading the target fibers is operated in Geiger mode.

---

[5] `http://www.hamamatsu.com/`

Chapter 4

Analysis

The specific analysis procedure described in this chapter focuses on track reconstruction inside the fiber target. In order to track the leptons through the magnetic fields of the spectrometer and measure the time-of-flight between TOF1 and TOF2 (see section 3.1.3), the outgoing angle of the lepton coming from the target needs to be known precisely.

In figure 4.1 a typical event is displayed as it is generated by the MC simulation (see section 2.3). Looking at it by eye, one can see a single track diverging into two separate tracks. One of them is stopping inside the target, the other one is apparently leaving it. Just calculating a linear fit on all bars would yield a bad result, if we are interested in the angle of the track leaving the target.

As described in section 2.4.1, a highly energetic lepton coming from the kaon decay can produce a knock-on electron. Being a lepton itself, it is also detected by the target fibers and leaves a secondary track branching off the actual primary decay lepton track. Because the goal of the analysis procedure is to find the outgoing angle of the primary track only, secondary tracks have to be identified and removed before fitting. This is the main problem the algorithm described in this section is trying to solve.

While the core algorithm had been previously designed and implemented, this thesis focuses on fixing bugs so that it would actually output usable data, improving its performance and quality, implementing measures to assess its accuracy and tune its parameters accordingly to optimize the results. These parameters will be marked as `PARAMETER` throughout the text. Improvements will be explained alongside the existing algorithm together with a study of their parameters' values in section 4.3. Supporting tools that were developed or extended during the improvement of the existing code are explained in section 4.2. A concise overview over the performance of the improved algorithm and the optimized parameters is given in section 4.4.

4.1 Overview

A brief overview over the algorithm is provided to give a sense of direction in the following, more in-depth sections. The individual steps are illustrated in figure 4.1.

1. **Separate the kaon and lepton tracks.** In figure 4.1 this separation has already

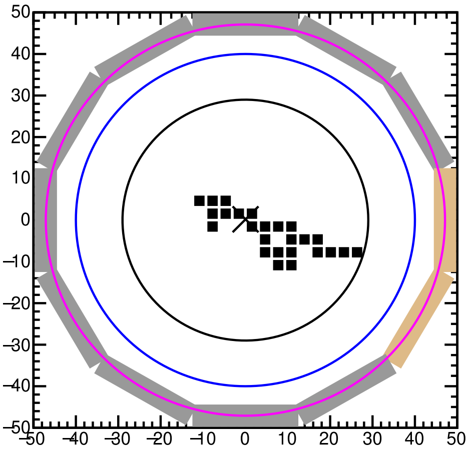

FIGURE 4.1: A typical event (`822/16`) as it is displayed by the `EventPlot` routine. Black bars inside the black circle indicate the fibers of the target that have been hit by a particle; the black cross is the center of the detector. The separation of the pixels into to diverging tracks is visible by eye. More details on the visualization are explained in section 4.2.1, but black is used for the individual bars to indicate their still indeterminate particle type.

taken place: the red lepton bars are displayed in subplot (Lepton Fit), the blue kaon bars in subplot (Kaon Fit). Details in section 4.3.1.

2. **Determine K-stop.** Determine the point where the kaon decayed into the leptons. The K-stop is shown in figure 4.1 subplot (K-Stop Determination) as a magenta asterisk. Details in section 4.3.2.

3. **Evaluate possibility of two leptons.** Calculate a preliminary fit for all lepton bars and decide, whether the event in question has two tracks or not. If it is a single track event, output the angle of the fit and terminate the algorithm. Otherwise continue with a two track analysis. Details in section 4.3.3.

4. **Separate lepton bars into two tracks.** Find the two tracks using the K-stop. Details in section 4.3.4.

5. **Assign lepton bars to the separated tracks.** Find the hit bars that form the two separate tracks. Figure 4.1 shows the separated tracks in subplots (Track 1) and (Track 2). Details in section 4.3.5.

6. **Choose the primary track.** Among the two tracks, identify the one that corresponds to the decay lepton and discard the knock-on electron track. The primary decay lepton track is shown in red inFigure 4.1 subplot (Both Tracks),

	interpreted	compiled
ROOT options	`.L` ⟨*program*⟩	`.L` ⟨*program*⟩`+`
events analyzed	51 458	51 458
total run time	202.65 s	83.17 s
	3:22.65 min	1:23.17 min
compared to compiled	2.44	1

TABLE 4.1: Comparison of the execution speed of a batch analysis between compiled and interpreted mode in the ROOT framework. The numbers were averaged over 5 runs. Execution takes over double the time in interpreted mode as it does in compiled mode.

whereas the secondary one is shown in green. Output the angle of the track and terminate the algorithm. Details in section 4.3.6.

4.2 Tools

4.2.1 Single Event Analysis

For the analysis of single events, the ROOT framework [6] version 6.08 was used. It is implemented in the C++ programming language and includes routines for fitting, numerical calculations and plot displays.

Besides other reasons, ROOT and C++ were chosen for speed. With the need to analyze tens of thousands of events, optimizing performance of a single event analysis becomes important. The main performance advantage of C++ is the fact that it is *compiled* language, which means that a program – the *compiler* – is used to translate the source code into machine instructions. ROOT offers a possibility to read and run C++ code interactively, where the statements are *interpreted* immediately, as opposed to being compiled and started as a separate program. While this allows for rapid testing and development and has been used extensively while working on the code, it comes with a big performance drawback.

One step forward in improving the existing code was to enable compilation by fixing various bugs and formulating statements in a more strict way. Before that, the analysis macros `Find_Many_Tracks_2.2.C`, used for single event analysis, and `Batch_Two_Tracks_Fit.C`, used for analyzing a big number of events in batch mode (see section 4.2.2), could only be used in interpreted mode. Table 4.1 shows the performance gained by using the compiled version.

The analysis macro `Find_Many_Tracks_2.2.C`, used by calling `FindTwoTracks()`, can be invoked with an option to produce a graphical display of the event and steps of the analysis algorithm. Such a display is shown in figure 4.2. Another big problem that was commonly encountered during the development, was the inflexible plotting mechanism. All plots were produced at the very end of the algorithm and could not be extended to temporarily show more information about a single step. On top of that, the fits shown in the plots were newly generated just for display. This has performance drawbacks but also gave birth to inconsistencies between the visual representation and the actual computation. Therefore, the plotting code was completely rewritten in a class called `EventPlot`, but kept the same visual appearance for consistency. It uses a more modular approach where elements like fits, bars, markers, arrows, or value output can be added at any point in the code to visualize data only accessible in that scope.

The `EventPlot` is used to inspect individual events and to find problematic ones which need adjustment in the algorithm. Coordinate axis describe the x- and y-direction perpendicular to the incoming beam and the units are given in mm. A black cross ($\times$) marks the center of the detector. The innermost black circle represents the core fiber target, which colored boxes marking hit bars. The blue circle shows the position of the SFT. As the outermost layer, the TOF1 counters are drawn as twelve gray boxes and a magenta circle. Counters have detected a hit are highlighted in a slight orange. The actual hit point in the TOF1, as reported by the simulation, is shown as a box in either red with error bars, or cyan. The point where the knock-on electron was emitted according to simulation data is shown as a small green box with a black line drawn towards the bar that has been hit last by the knock-on electron.The simulation K-stop is shown as a blue cross ($+$), whereas the algorithmically determined one is marked as a magenta asterisk ($*$). In the top row lepton bars and fits are represented in red and kaon bars and fits in blue. In the bottom row, red represents the primary decay lepton track and green the primary knock-on electron track.

4.2.2 Batch Analysis Evaluation

In order to find areas of improvement and spot problematic events systematically, statistics for a large number of events has to be generated.

The program `Batch_Two_Tracks_Fit.C` offers a function `Batch_Two_Tracks_Fit()`, which calls `FindTwoTracks()` on a whole data file with many individual events, and compiles the results. It can generate a PDF file with multiple `EventPlot` displays for faster inspection and has a non-graphical mode to generate Comma Separated Values (CSV) data files for further processing. A function `Multi_Batch()` to run CSV generation on multiple data files at once is also included.

The resulting data file includes many different output variables for each event for further analysis, including the angles of the primary and secondary track as well as their errors compared to the simulation data, the K-stop radius as well as its distance to the simulated one, lengths of tracks in the target as well as their energy deposit, the algorithm parameters, and one/two track analysis mode. This information is then read by a PYTHON[1] program which uses SCIPY [18] for statistical analysis and MATPLOTLIB [17] to produce a summary plot for a data file. An example of a meta-analysis summary plot is shown in figure 4.3.

Several cuts on the data are performed before further evaluation in order to remove erroneous events. Events which satisfy the following conditions were excluded.

---

[1] https://www.python.org/

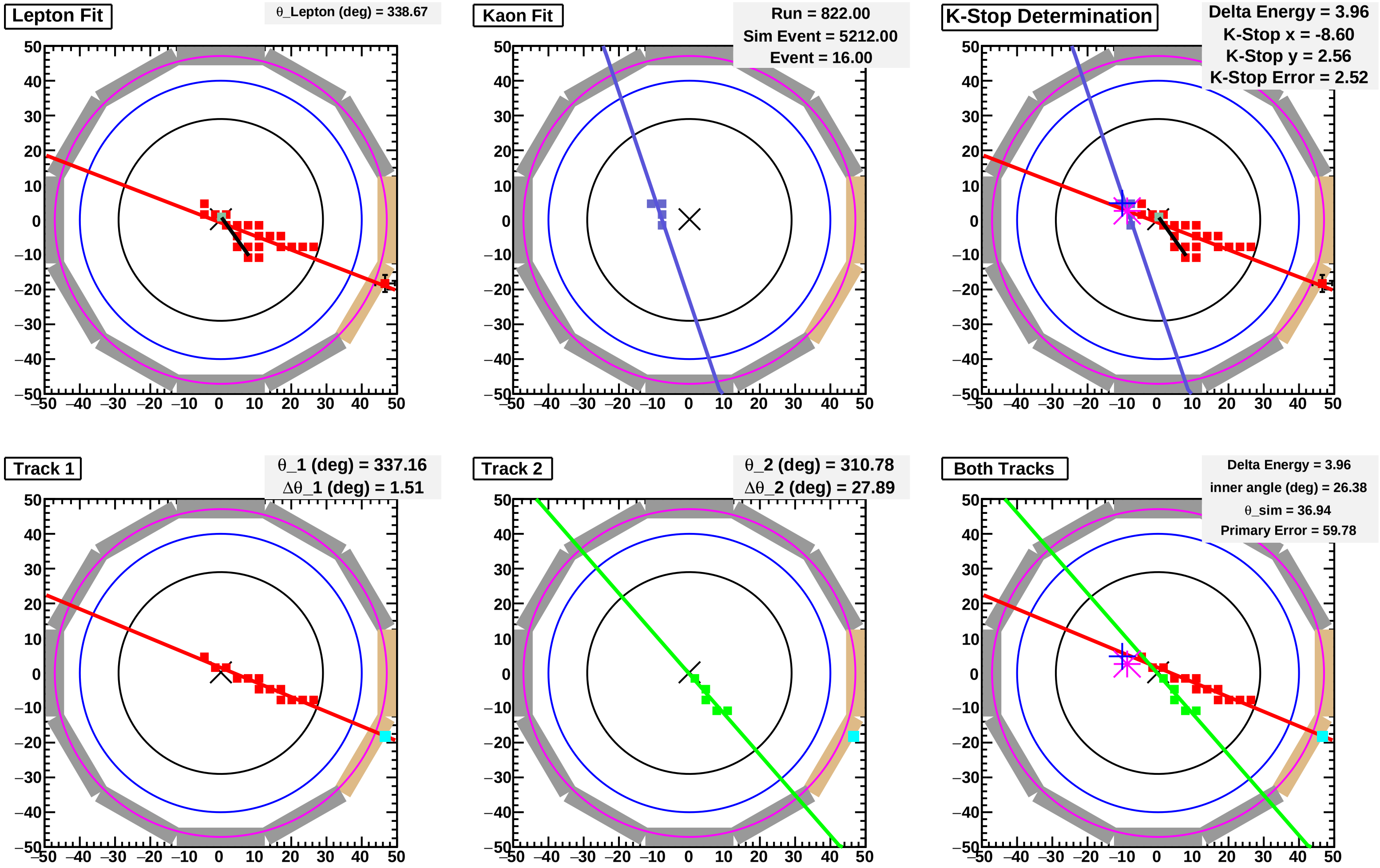

Figure 4.2: Display of an example event `822/16` as it is displayed by `EventPlot`. It is used to inspect individual events and visualize the analysis algorithm. The individual steps are outlined in section 4.1. More details on the visualization are explained in section 4.2.1.

run number	2161
number of events	5981
delta detection efficiency	82.29%
mean primary angle error	1.45°
mean difference one/two-track fit	3.20°
mean K-stop error	2.51mm
fraction events k_stop_error > 10	1.37%
fraction events angle_primary_error > 10	1.45%
events with missing tracks (kaon/lepton)	6.12%

TWO_TRACK_MIN_CHISQ	1.5
TWO_TRACK_MIN_LEPTON_BARS	5.0
FIT_TOF1_WEIGHT	3.0
K_STOP_CENTROID_THRESH	8.0
PATH_TRAVERSIAL_USE_ALL	1.0
PATH_TRAVERSIAL_DIJKSTRA_JUMP_RADIUS	9.0
PATH_TRAVERSIAL_ALL_PENALTY	1000.0

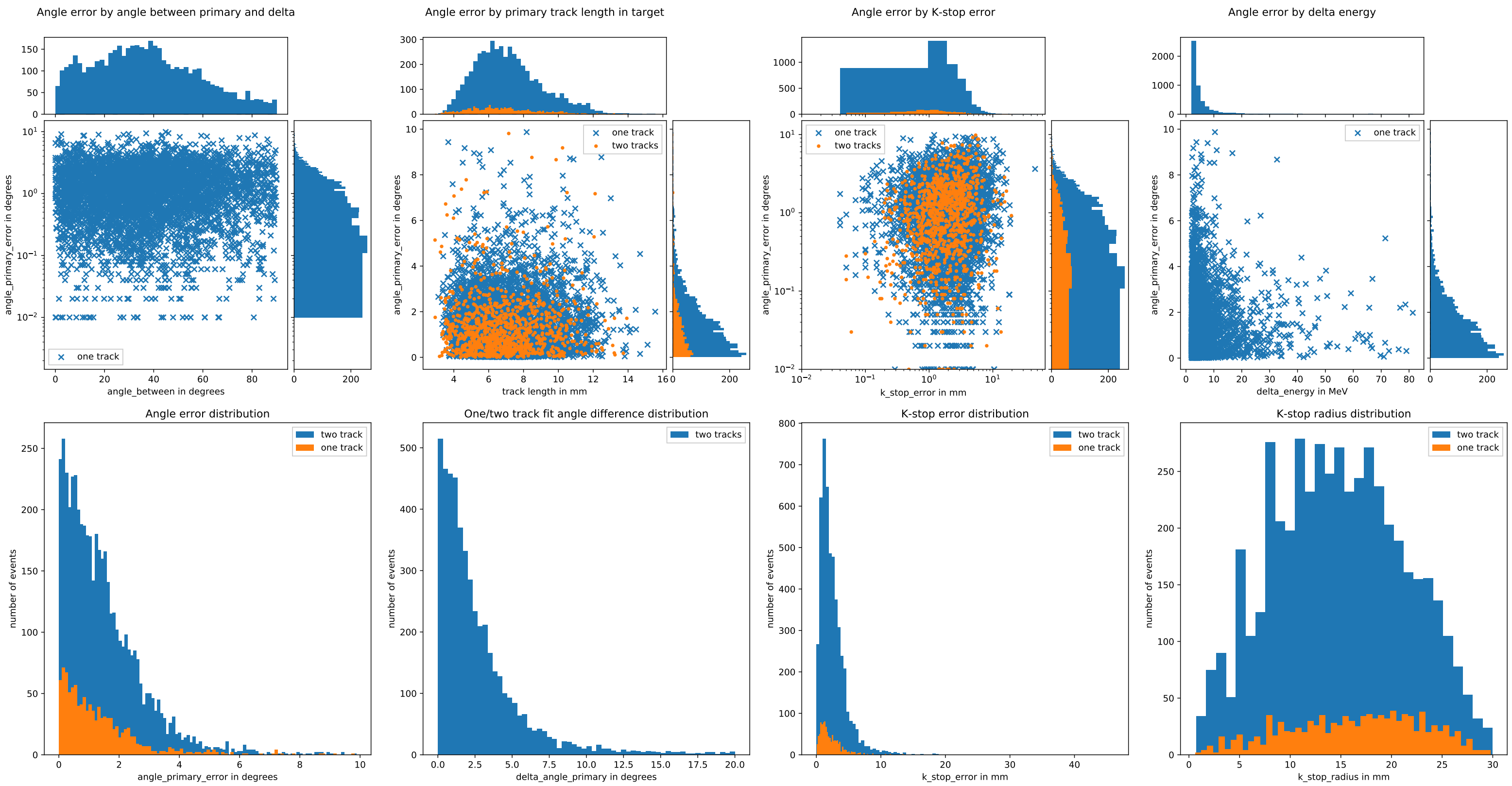

Figure 4.3: A summary plot of the meta-analysis of a data file with many events. The top-left table shows statistical data about all the events, the top-right table gives the values of algorithm parameters in this run. Below are graphical evaluations of the data. The top row shows scatter plots of different quantities with respect to the error in the primary angle determination (algorithm compared to simulation). Projections onto the axis are shown as histograms around the scatter plots and in the case of logarithmic plots, one has to take the logarithmic bin size into consideration. The bottom row displays distributions of different output quantities. Events were a two track fit was attempted are shown in blue, one track fits in orange. More information about the individual quantities is given in section 4.2.2.

- Missing lepton or kaon tracks. No analysis can be performed on them.
- K-stop error greater than 100 mm. Keep in mind, that the target itself is only 60 mm in diameter (see section 3.2). These are mostly events where the K-stop reported by the simulation is wrong and cannot be compared to the algorithmically determined one (see also section 4.3.2).
- Primary angle error greater than 10°. The majority of these events have a wrong simulation angel.
- Energy of the knock-on electron negative or greater than 120 MeV. These are very irregular events and are artifacts of a bug in the simulation or single event analysis.

Lists of all excluded events are sorted and output to identify problematic events and fix or tune the algorithm accordingly.

Quantities and variables used in the plots are the following. Means have been calculated with `numpy.mean()`[2] as $1/N \sum_i^N x_i$. All these values are only calculated for two track events, unless otherwise stated.

run number Internal identifier of the data file.

number of events The total number of events analyzed for this plot after the cuts have been applied.

delta detection efficiency The fraction of events in this data set which has been identified as two track events.

primary angle error Absolute value of the difference between the primary decay lepton angle as reported by the algorithm and the simulation. Given in degrees.

primary angle error std deviation The standard deviation of the primary angle error over the whole data set. It is calculated with `numpy.std()`[3] which evaluates $\sqrt{1/N \cdot \sum_i^N (x_i - \bar{x})^2}$, where $\bar{x}$ is the mean value of x (see above). This helps do understand the spread of the angle error.

difference one/two-track fit For events with two tracks, the difference between the calculated primary angle for fitting all bars as one track and using the two track algorithm is calculated.

fraction events k_stop_error > 10,
fraction events angle_primary_error > 10,
events with missing tracks (kaon/lepton)
Fractions of events excluded by the cuts described above. For the primary angle error, the cuts are performed for more than 100 mm, but the fraction for more than 10 mm is shown as an indicator of “bad” events.

---

[2] https://docs.scipy.org/doc/numpy-1.14.0/reference/generated/numpy.mean.html

[3] https://docs.scipy.org/doc/numpy-1.14.0/reference/generated/numpy.std.html

angle between primarty and delta The acute angle between the primary and secondary tracks. This is included because it is interesting to see whats the minimal angle between two tracks that the algorithm can resolve and how its performance is dependent on it.

primary track length in target The length of the primary lepton track inside the target as reported by the simulation. Longer tracks produce better fits and the dependence of the algorithm on the length is to be studied.

K-stop radius The euclidean distance between the K-stop found by the algorithm and the target center. Analyzed to check anomalies in K-stop determination.

delta energy The energy deposited in the detector by the knock-on electron as reported by the simulation. Lower energies could affect the algorithms performance,

Descriptions on the parameters listed in the top-right table are given in the respective section in section 4.3.

4.2.3 Parameter Variation

In order to study the influence of algorithm parameters and optimizing their values, a automated way to varying them was created.

The tunable parameters are defined in a special header file called `TweakParameters.h`. A PYTHON program called `parameter_study.py` accepts a list of parameters and ranges to vary them. For every parameter and variation, a header file is generated and the batch analysis `Batch_Two_Tracks_Fit()` is run on it, which analyzes a number of data files. Default values are used for all other parameters than the one being varied in a specific variation run. The meta-analysis PYTHON routine is then run on the resulting CSV files and the values listed in its output's top-right table are recorded for every variation. These figures of merit are then plotted in a summary plot as shown in figure 4.4

The following figures of merit are studied to improve the algorithm. For their detailed description, refer to section 4.2.2.

Mean Primary Angle Error This is obviously the strongest indicator for improving the algorithm. The y-values are given in degrees.

Primary Angle Error Standard Deviation Gives the spread or uncertainty of the primary angle error. The y-values are given in degrees.

Fraction of Events w/ Primary Angle Error $> 10°$ As an indicator on how many events are analyzed in a bad way, this is another important indicator. The y-values are given in degrees.

Delta Detection Efficiency How well the algorithm detects two track events is important. Data sets marked as "only deltas" show the true detection rate, for "mixed" sets, this quantity is meaningless. The data set marked as "no deltas" serves as a test for *false positives*. It includes no events with knock-on electrons, so the

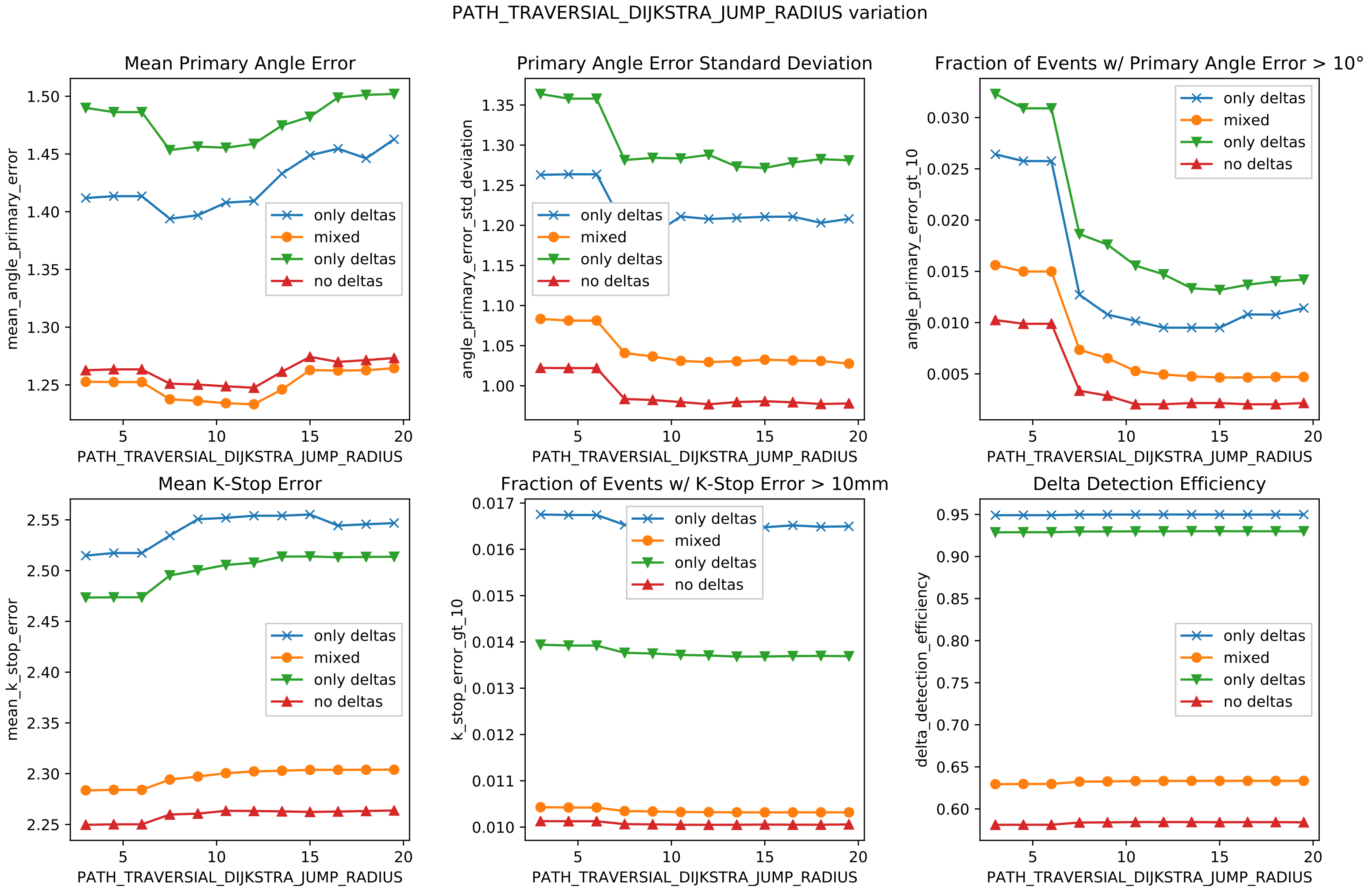

Figure 4.4: A summary plot of the dependence of the algorithm performance on a parameter (in this case `PATH_TRAVERSIAL_DIJKSTRA_JUMP_RADIUS`). The legend gives details about the forced amount of two track events in the respective data file. More information about the individual figures of merit is given in section 4.2.3.

detection rate shows how many events are wrongly identified. This is not very problematic, as one track events will yield a good two track fit as well. The y-axis is dimensionless.

Mean K-Stop Error Included to study the performance off the K-stop determination step of the algorithm (see section 4.3.2). The y-values are given in millimeters.

Fraction of Events w/ K-Stop Error > 10 mm Analogues to the primary angle error case, this shows the number of bad events. The y-axis is dimensionless.

The following data sets were chosen for the parameter studies.

`828` **(blue, “only deltas”)** Only events with knock-on electrons. In this data set, the correct angle for the outgoing decay lepton was not reported by the simulation. Therefore the angle of the line connecting the simulation K-stop and TOF1 hit point was used as a reference point. This data set only includes events with at least TOF1 hit energy between 150 MeV to 240 MeV. The knock-on electron has to have a minimum energy of 2 MeV and a minimum track length of 1.0 cm.

`214-1` **(orange, “mixed”)** Both events with and without knock-on electrons are included. The angle is reported by the simulation. Only events with at least one TOF1 hit are included.

`216-1` **(green, “only deltas”)** Only events with knock-on electrons from positrons, apart from that same restrictions as for set `828`. The angle is reported by the simulation.

`321-2` **(red, “no deltas”)** No events with knock-on electrons. More precisely, no constraints on TOF1 hit number were enforced, but no hits with energy larger than 200 MeV are allowed. Maximum knock-on electron hit energy is forced below 0.1 MeV and the track length below 0.5 cm. Serves as a survey of false positive rates. The angle is reported by the simulation.

4.3 Two Track Algorithm

4.3.1 Kaon/Lepton Separation

The algorithm receives an array of hit bar IDs with corresponding hit time and energy deposit. As a first step, these have to be classified as hit by either a kaon or a lepton.

After it hit the target and is slowed down, the kaon exists for a while at a constant position in the x-y-plane, before it decays into the lepton. Therefore, there is some time separation between the kaon and lepton hits. In the simulation data sets, the kaon hits usually happened in under 3 ns, and the first subsequent lepton hits started around 5 ns the earliest, often even at more than 10 ns. Even though the energy deposit for kaon hits is usually higher, partially hit bars still detect a low energy deposit comparable to the lepton bars, so it is not suitable to use the energy information at this point. The timing information is sufficient for most cases.

To clean up the data, hits with a minimum energy of less than currently 0.03 MeV are discarded.

From the remaining bars, the minimum time t_{min} and maximum time t_{max} are determined. They are averaged over the two smallest and two largest timing values, respectively. Using these, a separation step width t_{step} is calculated as the midpoint between these two values

$$t_{\text{step}} = \frac{1}{2}\left(t_{\text{max}} - t_{\text{min}}\right) . \tag{4.1}$$

As mentioned earlier, the timing offset between the two particle types is usually large enough that the midpoint separates both types cleanly. However, if $t_{\text{step}} < 0.5\,\text{ns}$, then the time separation is considered to small to accurately discriminate particles and the algorithm flags these events as unprocessable.

In case the difference between the two minimal or two maximal timings is larger than the step size, $t_{\text{min},2} - t_{\text{min},1} > t_{\text{step}}$ or $t_{\text{max},1} - t_{\text{max},2} > t_{\text{step}}$, only the second to extremum values will be used for $t_{\text{min,max}}$; t_{step} has be recalculated accordingly. This discards outlier extremum values.

For each bar with time t, its timing difference to the minimal value Δt, i.e, the offset from the first hit, is be calculated

$$\Delta t = t - t_{\text{min}} . \tag{4.2}$$

This offset is now compared to the step width and the bar classified accordingly, leptons being in the later half of the interval, kaons in the earlier one.

$$\begin{aligned} t_{\text{step}} < \Delta t < 70\,\text{ns} \quad &: \text{lepton}\,, \\ -0.1\,\text{ns} < \Delta t \leq t_{\text{step}} \quad &: \text{kaon}\,. \end{aligned} \tag{4.3}$$

The numerical constrains filter erroneous events.

4.3.2 Kaon Stop Determination

After separating the tracks, the point where the kaon ceased to exist and decayed into the charged lepton and neutrino, needs to be determined. This point is called “K-stop”.

The K-stop was mainly determined by taking the intersection point of fits for kaon and lepton bars. In the optimal case, this yields the exact point where both trajectories intersect, which has to be the origin point of the lepton. For the fits, the ROOT function `TGraphErrors::Fit()`[4] is used with a first degree polynomial (line) and takes the uncertainties of the bars into account. The lepton bars include the (simulated) TOF1 hit multiple times according to `FIT_TOF1_WEIGHT`. They are first fitted without error bars to get a good guess for the slope and intercept parameters of the line fit, and then again taking the error bars into account.

As it can be seen in the meta-analysis in figure 4.5, there seems to be a correlation between K-stop error and primary angle error, so it is worth improving the K-stop

---

[4] https://root.cern.ch/doc/v608/classTGraph.html#aa978c8ee0162e661eae795f6f3a35589

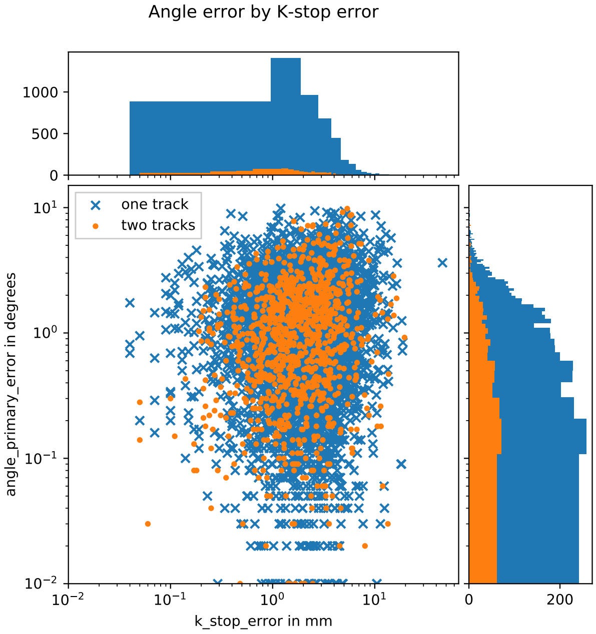

Figure 4.5: Excerpt from the meta-analysis of run `216-1` to show the correlation between K-stop error and primary angle error. Details on graph generation in section 4.2.2.

determination. In the original algorithm, the distribution of K-stop errors looked like in figure 4.6a. The long tail which stretches out towards the cutoff 100 mm is noteworthy. It has a non negligible proportion above 20 mm, which is still a third of the target diameter.

After inspecting a number of events with big K-stop error, the source of the problem was found. As illustrated in figure 4.7, a wide spread in the lepton bars – most likely they contain two tracks – leads to an intersection point far off any hit bars. The K-stop has to be near the kaon bars, even if there is some gaps in the lepton bars. To enforce that, some changes were made to the algorithm.

If the x-y-spread of the kaon bars is more than 6.2 mm (roughly two bars), the same intersection method is tried. If the intersection point's radius lies within the target or SFT, and its distance to any kaon bar is less than `K_STOP_CENTROID_THRESH`, it is accepted as the K-stop.

Otherwise, the centroid of the kaon bars is calculated by summing all x- and y-coordinates, respectively, and dividing by the number of bars. If there are kaon bars with an energy deposit of $E > 1\,\mathrm{MeV}$ and a time of hit $t < 3\,\mathrm{ns}$, then only these are used. Otherwise all kaon bars are used.[5]

With the new method, the K-stop is now placed closer to the actual one, as it can be seen (magenta asterisk) in figure 4.7. The comparison in figure 4.6 shows clearly, that the new method improves with a `K_STOP_CENTROID_THRESH` of 8 mm.

---

[5] Minimum energy and maximum time would also be suitable parameters for systematic variation.

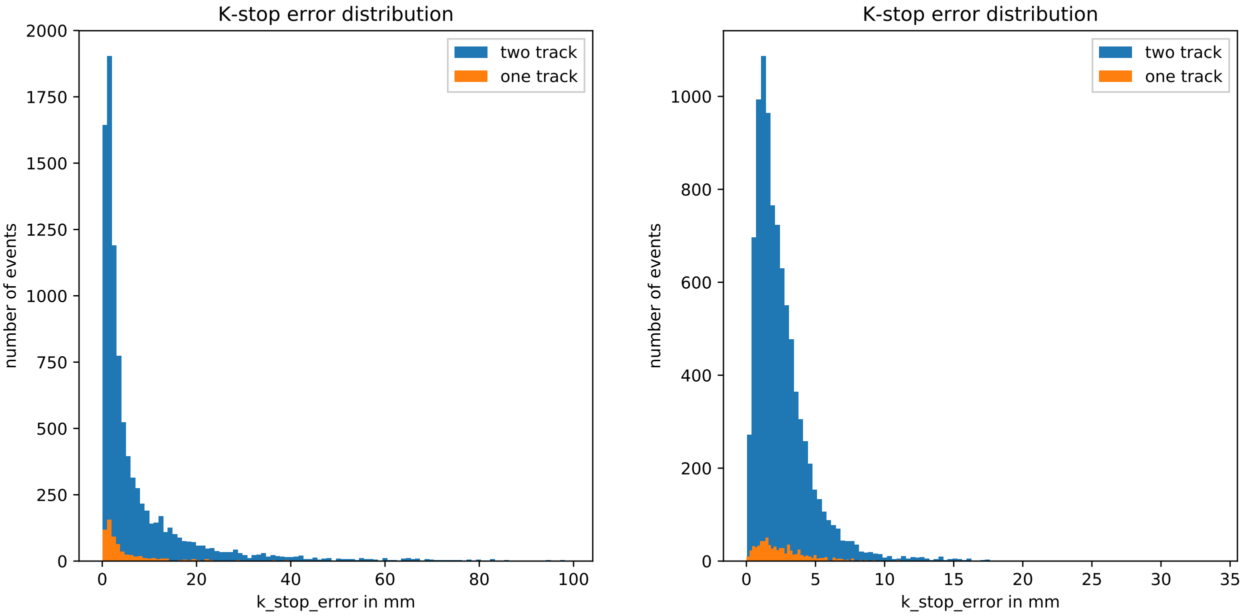

(a) Before the improvement. Significant number of events with K-stop error over 20 mm

(b) After the improvement. The number of events with K-stop error over 20 mm is negligible.

Figure 4.6: A comparison between the old and new method of determining the K-stop on run `1212-1`. The new method significantly decreases the amount of events with large K-stop error (note the x-axis scale). Details on graph generation in section 4.2.2.

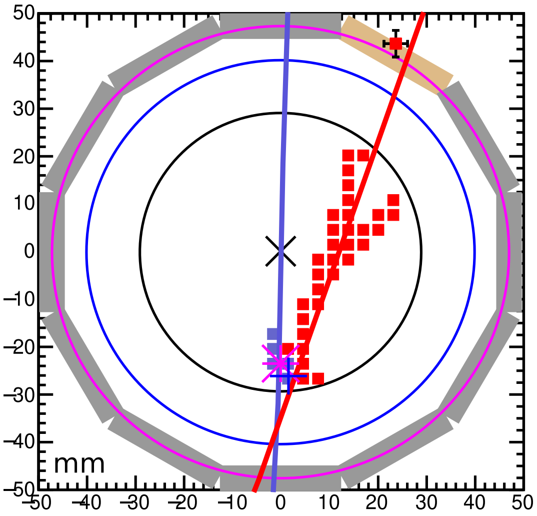

Figure 4.7: Illustration of the problem with the intersection method for determining the K-stop (event `828/1`). Because of the spread in the lepton bars, the intersection point is far off. The centroid is the better solution. For details on the graphs elements, refer to section 4.2.1.

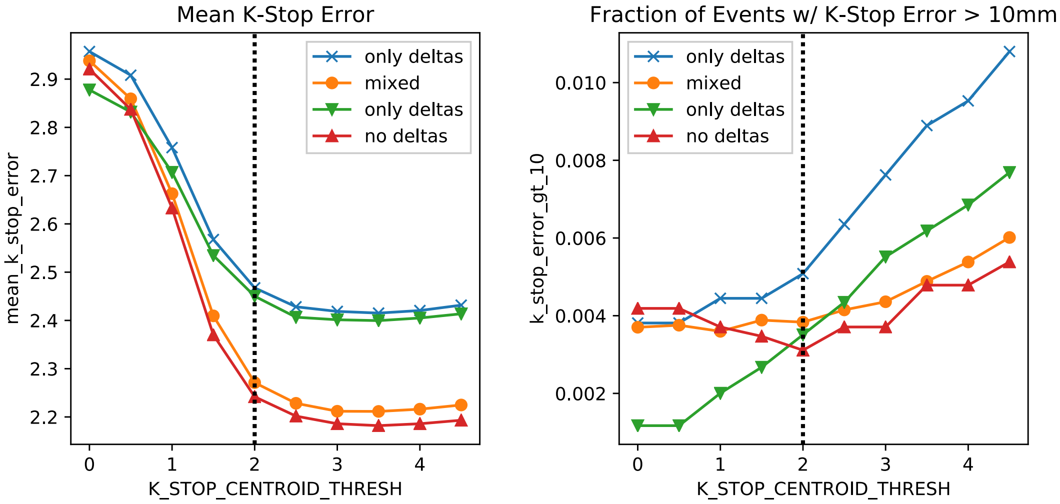

FIGURE 4.8: The influence of the variation of the parameter `K_STOP_CENTROID_THRESH` on the K-stop. The value that minimizes both mean K-stop error (left) and number of bad events (right) is shown as a dotted line. K_STOP_CENTROID_THRESH is given in mm. Details on graph generation in section 4.2.3.

The threshold distance to the kaon bars `K_STOP_CENTROID_THRESH` has been varied according to section 4.2.3, to find the optimal value. Figure 4.8 shows its influence on the K-stop. While the mean K-stop error remains mostly constant beyond 2 mm to 2.5 mm, the fraction of bad events increases for most data files at least beyond 2 mm. Therefore 2 mm is chosen as the optimal value for `K_STOP_CENTROID_THRESH`.

4.3.3 Two Track Decision

After the K-stop has been found, the algorithm tries to decide, whether the event in question includes a knock-on electron and a two track fit has to be performed or all lepton bars can be considered part of one track.

As a first requirement for performing a two track fit, the number of lepton bars has to be greater than `TWO_TRACK_MIN_LEPTON_BARS`. If there is too few bars, the algorithm will not be able to resolve the different tracks, even if they were present. In that case, a single track fit would still yield better results.

This parameter has been varied according to section 4.2.3 to find the best value for the minimum number of bars. Figure 4.9 shows, that for values greater than 2, the mean primary angle error and its standard deviation remain mostly stable, indicating that even the mathematically minimal number for a fit yields good results results. As the value is increased, too few events are tried to be evaluated as two track events and the number of bad events rises. The efficiency is not very dependent on this parameter, but the false positive rate (as indicated by the red line) peaks at 2. This is not really problematic, as one track events will yield good fits when evaluated via the two track routine as well. Therefore, 2 was chosen as the optimal value.

Aside from this technical constraint, the actual question of judging the two-track-nature of the event needs to be addressed. For the fit of all lepton bars obtained during K-stop determination (section 4.3.2), a quantity called *reduced loss* $\ell^\star$ is calculated as follows.

The *loss* ℓ is the sum of squared distances for each point (lepton bar) from the line of the fit. If the world space coordinates of the N bars are given by (x_i, y_i) for $i = 1, \dots, N$ and the line fit is parameterized as $y(x) = mx + t$ with slope m and intercept t, then

$$\ell = \sum_{i=1}^{N} \left[d\left(x_i, y_i, m, t\right) \right]^2 . \tag{4.4}$$

Here d is the shortest distance between a point and the line as given by

$$d\left(x, y, m, y\right) = \frac{|-mx + y - b|}{\sqrt{m^2 + 1}} . \tag{4.5}$$

The reduced loss is obtained by dividing the loss by the number of degrees of freedom n_{df} of the line fit.

$$\ell^\star = \frac{\ell}{n_{\mathrm{df}}} . \tag{4.6}$$

The number of degrees of freedom for a fit is returned by ROOT's `TF1::GetNDF()` function. It is defined as “The number of degrees of freedom corresponds to the number of points used in the fit minus the number of free parameters”.[6] In this case the number of free parameters, m and t, is 2.

Now the reduced loss is used as a measure of spread in the lepton bars. If the spread is too big, i.e., $\ell^\star >$ `TWO_TRACK_MIN_CHISQ`, the event is considered to have two tracks and the algorithm continues with the two track procedure. A single lepton should lead to a mostly straight line of hit bar and therefore have a small $\ell^\star$. In that case the algorithm terminates and outputs the angle obtained from the linear fit of all lepton bars.

`TWO_TRACK_MIN_CHISQ` has been varied systematically according to section 4.2.3 with the results shown in figure 4.10. Obviously the detection efficiency decreases with increasing parameter value, and so does the false positive rate (indicated by the red line). As the number of bad events is only mildly affected, the drop in mean primary angle error and its standard deviation for mixed and no delta data sets, and in the false positive rate, motivate the choice of 1.5 mm^2 (reduced).

4.3.4 Lepton Track Separation

For events that have been evaluated as having two tracks because of a knock-on electron, the core problem of separating both lepton tracks has to be solved.

---

[6] https://root.cern.ch/doc/v608/classTF1.html#a0ec4878f851604ca6130832b561e2d81

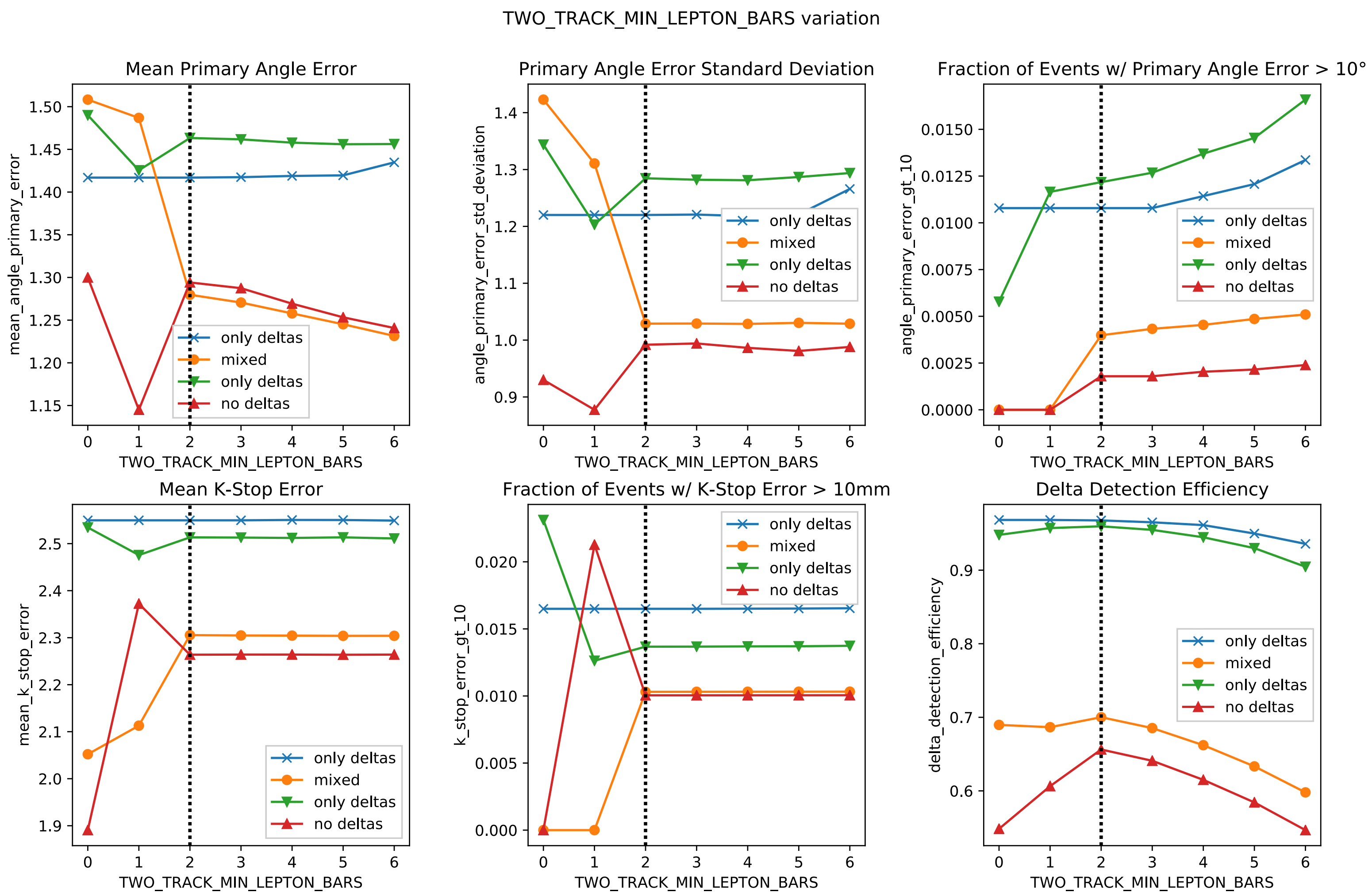

Figure 4.9: The influence of the variation of the parameter `TWO_TRACK_MIN_LEPTON_BARS` on the algorithm performance. Trying to reduce the mean primary angle error, its standard deviation, and number of bad events while keeping the efficiency high results in an optimal value chosen as indicated by the dotted line. Details on graph generation in section 4.2.3.

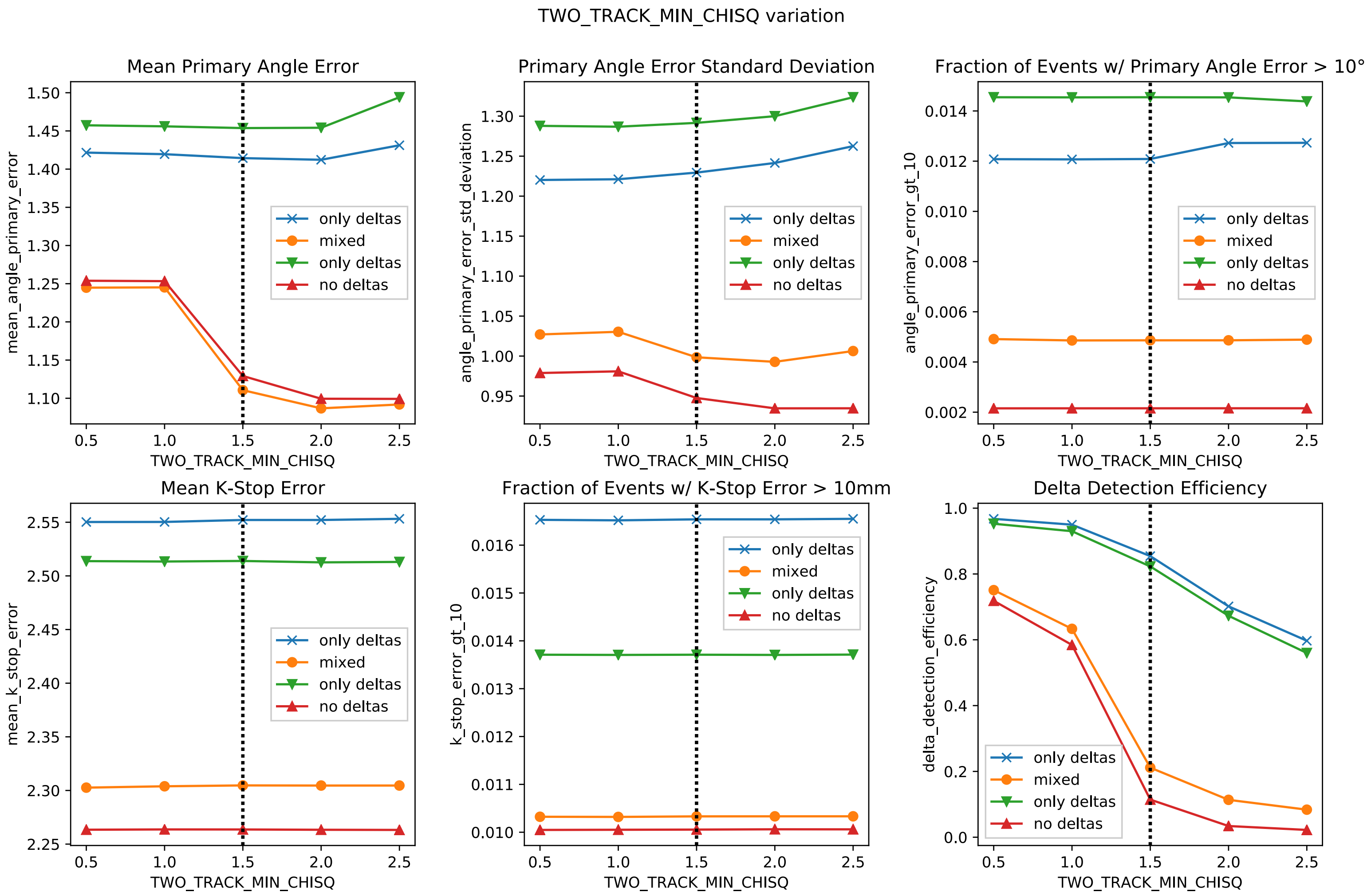

Figure 4.10: The influence of the variation of the parameter `TWO_TRACK_MIN_CHISQ` on the algorithm performance. Trying to reduce the mean primary angle error, its standard deviation, and the number of bad events while keeping the efficiency high results in an optimal value chosen as indicated by the dotted line. TWO_TRACK_MIN_CHISQ is given in mm^2 (reduced). Details on graph generation in section 4.2.3.

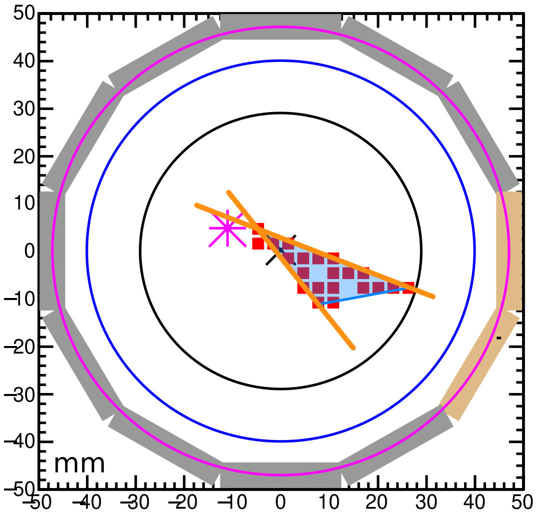

FIGURE 4.11: Illustration of the concept of track separation by using a triangle covering the lepton tracks. Adapted from event `822/16`. The triangle of largest area covering the lepton tracks is shown in blue. The sides of the triangle going outward from the K-stop (magenta asterisk) shown in orange constitute the two separated tracks. For details on the graphs elements, refer to section 4.2.1.

The main idea is that the knock-on electron is emitted at a certain angle to the primary lepton track, therefore roughly forming a triangle with the K-stop and the outermost lepton bars for each track as the corner points. Figure 4.11 illustrates the concept. As the knock-on electron emission angle can be assumed to be acute, both particles go outward from the K-stop, because it is the point of origin for the primary lepton. Both tracks will then be the sides of the triangle connecting the K-stop with the outer most points of each track. For events where the knock-on electron emission happens far away from the K-stop and its bars would not align with the side of the triangle, this still works because of how the actual bar track is constructed from these lines (see section 4.3.5).

Now, the three bars that span the triangle of largest area have to be found.

As a first step, the *convex hull* of all lepton bars is determined. A convex hull of a set is the smallest convex polygon containing all points in that set. A polygon is a set of points joined by line segments that covers a closed area. Convex means that that all line segments connecting all possible pairs of points in the polygon lie within the area covered by the polygon. To find the convex hull, the *Graham scan* [14, 12] algorithm is used. Details are provided in the references.

From the set of bars in the convex hull, all permutations of sets of three bars are considered and the area covered by the triangle connecting the world positions of the respective bars is calculated. The three bars with the largest associated triangle area are chosen as the corner bars.

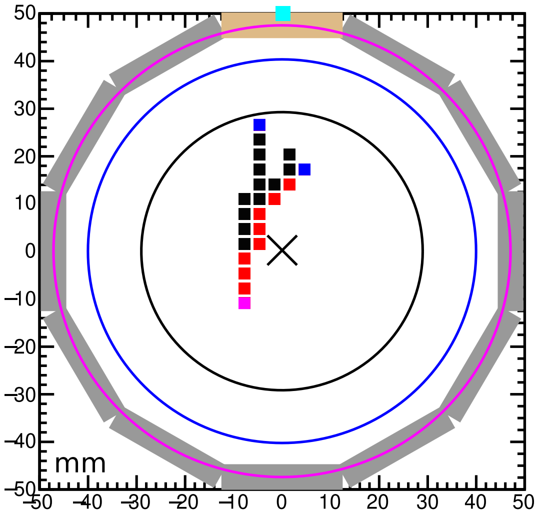

FIGURE 4.12: Illustration of a path (red) through adjacent lepton bars (black) connecting the corner bar closest to the K-stop (magenta) to one of the other corner bars (blue). Adapted from event `1213-1/6013`. For details on the graphs elements, refer to section 4.2.1.

Two lines connecting the bar with the world position closest to the K-stop with each of the remaining two bars are defined. These lines roughly correspond to the two tracks of the two leptons. The next section will be concerned with assigning the hit lepton bars to either of the lines and therefore forming the actual tracks.

4.3.5 Bar Assignment

To find the actual bar tracks that are associated with the lines found in the previous step, two paths of bars that connect the corner bar closest to the K-stop with each of the two other corner bars, have to be constructed. This is illustrated in figure 4.12.

The goal is to find a path through a set of connected bars. Therefore the bars are represented as an *undirected graph*. This is not to be confused with a graphical visualization of a function. A graph is a set of points called *vertices* or *nodes*. Pairs of vertices can be connected by *edges* which represent some sort of relation between the respective vertices. In a *weighted graph*, the edges have an associated numerical value, the *weight*. It is used to quantify the relationship between the connected vertices.

Each hit lepton bar is a vertex of the graph and has edges to each of its eight adjacent neighbor bars, but only hit bars are considered. The weight of the edges is taken to be the euclidean distance between the world space coordinates of each bar. Therefore diagonally adjacent bars have a higher weight than orthogonally adjacent ones.

To find the connection between two points in this graph, namely the bar closest to the K-stop and one other corner bar, *Dijkstra's algorithm* [8] is used. Given a source vertex, it computes the shortest path to every other vertex by choosing a path through vertices which minimizes the sum off the weights along the path. For details refer to the literature. The lepton paths are now the shortest paths between the corner bar closest to the K-stop, and one of the remaining corner bars.

Not only the lepton hit bars that are part of the shortest path should be part of the track. Therefore, all lepton bars that are adjacent to only one of the paths are added to the respective track. The resulting clean up of the tracks, where bars far from the paths are excluded, can be seen in figure 4.2 comparing (K-Stop Determination) and (Both Tracks).

This method has a problem with events that have gaps in their lepton bars, i.e., not all chunks of lepton bars are adjacent to each other. An example of such an event can be seen in figure 4.13

Gaps in the bars can have multiple origins. Fibers have a finite detection efficiency; therefore, one fiber along the lepton trajectory through the target might simply not detect a hit. Some events have kaon bars overlapping with lepton bars, because secondary electrons are emitted by the kaon before the decay. Of course these should not be considered for the track fitting. Same is true for single outlier bars that light up in the detector because the are for example struck by cosmic radiation. As such processes are not implemented in the simulation, they are not of concern for this analysis, but experimental data has to be cleaned accordingly before analysis.

Jumping

The way to handle gaps in the lepton bars, that was implemented, is to allow Dijkstra's algorithm to "jump" over gaps while searching for a path. If it finds a bar that does not have any edges to other vertices in the graph, it adds all hit bars within a certain world space radius as vertices connected to that bar to the graph. Figure 4.13 illustrates this behavior.

Originally a radius of 9 mm was set. That corresponds to three bars orthogonally an roughly two bars diagonally. In order to find the best value for this the jumping radius was made a parameter, `PATH_TRAVERSAL_DIJKSTRA_JUMP_RADIUS`. Now the parameter was varied as described in section 4.2.3 with the results presented in figure 4.14.

The number of bad events and the primary error standard deviation has a big decrease after 7.5 mm and continues to decline more slowly afterwards. While it might seem desirable to increase the radius even higher, this worsens the mean primary angle error, which has its minimum at 7.5 mm. So this value was chosen as the optimum.

Off-Track-Penalty

Jumping over large distances has the problem of including bars that are within the radius, but skipping other bars that should be traversed as part of the path. Therefore a different method of handling gaps was implemented as part of the work on this thesis.

In this method, not only hit lepton bars, but *all* adjacent bars are considered to be connected by edges in the graph. To only use non-hit bars in a gap and not for the whole path, walking through non-hit bars is penalized by artificially scaling the weight of the associated edge. This makes it "cheaper" for the algorithm to walk through hit bars and

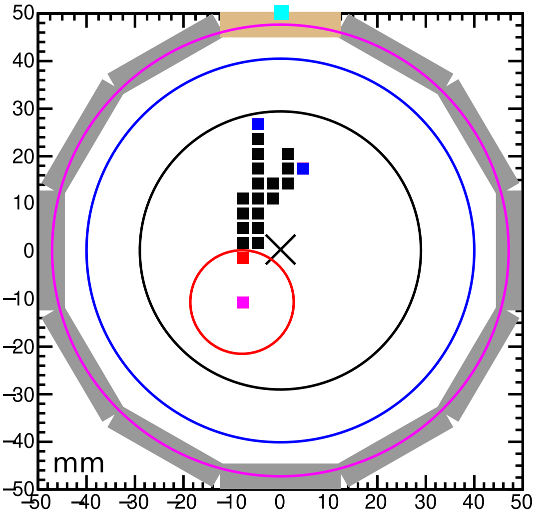

FIGURE 4.13: Illustration of the jumping method to deal with gaps in lepton bars during track construction. Adapted from event `1213-1/6013`. Lepton bars are shown in black, with the bar closest to the K-stop in magenta, the other corner bars in blue. Red bars are part of the constructed track. The red circle indicates the radius in which non-adjacent bars are considered for bars without neighbors. For details on the graphs elements, refer to section 4.2.1.

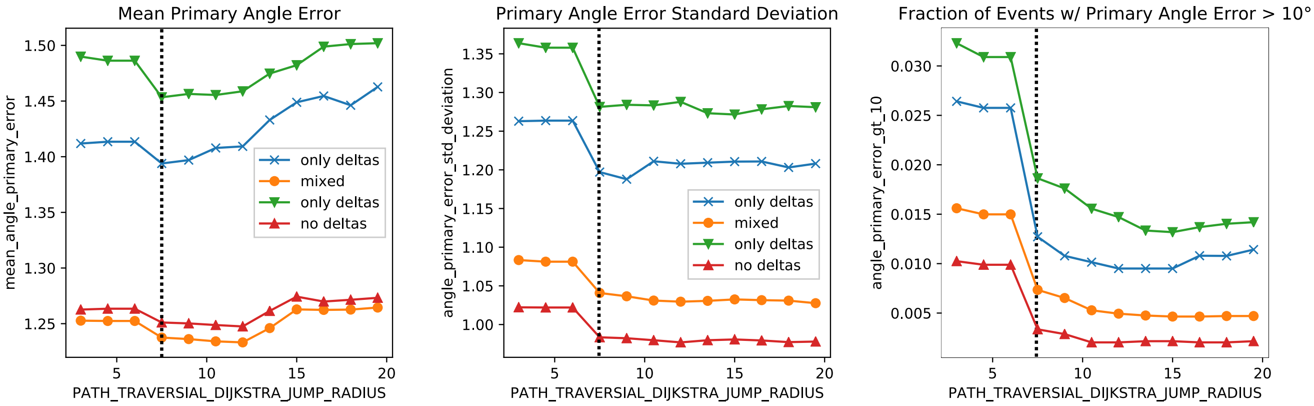

FIGURE 4.14: The influence of the variation of the parameter `PATH_TRAVERSAL_DIJKSTRA_JUMP_RADIUS` on the primary angle error. The value 7.5 mm minimizing primarily the mean primary angle error and its standard deviation, but also reducing the number of bad events significantly is shown as a dotted line. PATH_TRAVERSAL_DIJKSTRA_JUMP_RADIUS is given in mm. Details on graph generation in section 4.2.3.

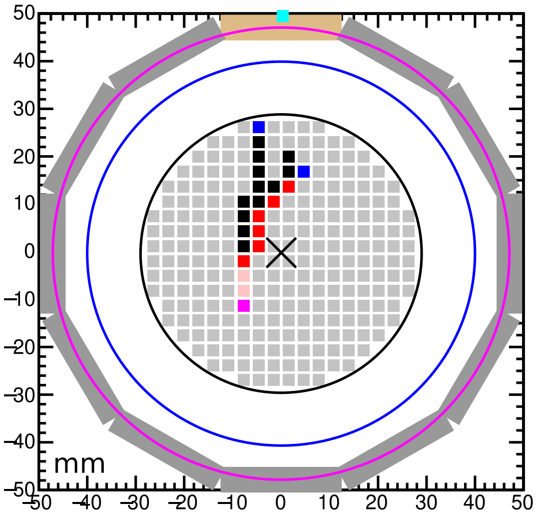

Figure 4.15: Illustration of allowing non-hit adjacent bars during track construction in order to deal with gaps in the lepton bars, but penalizing them. Adapted from event `1213-1/6013`. Lepton bars are shown in black, with the bar closest to the K-stop in magenta, the other corner bars in blue. Red bars are part of the constructed track. Translucent bars indicate that their weight has been artificially increased. For details on the graphs elements, refer to section 4.2.1.

the path will immediately snap to these if they are available. Figure 4.15 illustrates this behavior.

The penalty on the edges is enforced by multiplying their original world space distance value with `PATH_TRAVERSAL_ALL_PENALTY`. This parameter has been varied as described in section 4.2.3 and the results are shown in figure 4.16.

As one would expect, once the penalty is above a certain threshold, the actual value has no influence anymore. It is strong enough to force the path back onto the hit bars immediately while allowing jumps over gaps of arbitrary size. Any value above 10 seems to be sufficient, 1000 has been set as a default value.

On all data sets the jumping method was very slightly better in terms of the mean primary angle error and its standard deviation, but slightly worse in terms of the detection efficiency. Ultimately the angle error matters most, hence, the jumping method was chosen as the default.

4.3.6 Primary Identification

Having separated and populated the two tracks, the one corresponding to the primary decay lepton has to be identified and the one corresponding to the knock-on electron marked as secondary. Only the primary track is energetic enough to reach the TOF1, so the primary track should be the one aligned with the TOF1 hit point.

Originally this was determined by considering the reduced χ^2 of fits of each track

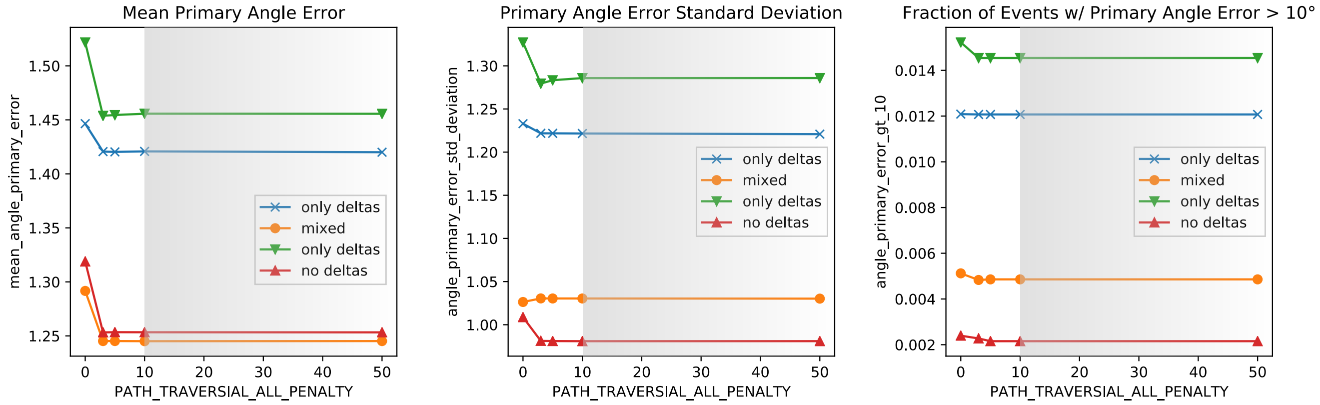

FIGURE 4.16: The influence of the variation of the parameter `PATH_TRAVERSAL_ALL_PENALTY` on the primary angle error. Above a certain value, the penalty is strong enough and the actual value does not have an influence anymore. Acceptable values are covered in gray. Details on graph generation in section 4.2.3.

including the TOF1 hit point. For a set of points $\{(x_i, y_i)\}$ and a fit function f, χ^2 can be calculated by [35, eqn. 42]

$$\chi^2 = \sum_i \frac{\left(y_i - f(x_i)\right)^2}{\sigma_i^2}\,, \tag{4.7}$$

where σ_i is the Gaussian uncertainty associated with the value of y_i. To find the reduced χ^2, it has to be divided by the number of degrees of freedom. The track with the lower χ^2 value is the better fit for the track including the TOF1.

This method failed for events with a big spread in the primary track and a well aligned secondary track, like the one displayed in figure 4.17. Even taking the TOF1 into account, which is far off from the perspective of the secondary track, the fit for the spread out primary bars results in the greater χ^2 value.

To improve the identification method, two fits are now calculated for each track. One including the TOF1 hit, and one with out it. The track with the smaller angle difference between these two fits is identified as the primary one. This way, the algorithm does not have to care about the χ^2, i.e., the spread of the track, but directly selects the one “more in line” with the TOF1 hit point.

The weight, with which the TOF1 is included in the fit is varied with the parameter `FIT_TOF1_WEIGHT`. This is simply achieved by adding it multiple times to the data set before fitting. To study the impact of the TOF1 weight on the algorithm, it has been varied according to figure 4.18.

As expected, not including the TOF1 in the fits yields very bad results on all metrics. Generally any figure or merit only seems to get better with a higher weight for the TOF1. Unfortunately this result does not transfer over to the analysis of experimental data, as

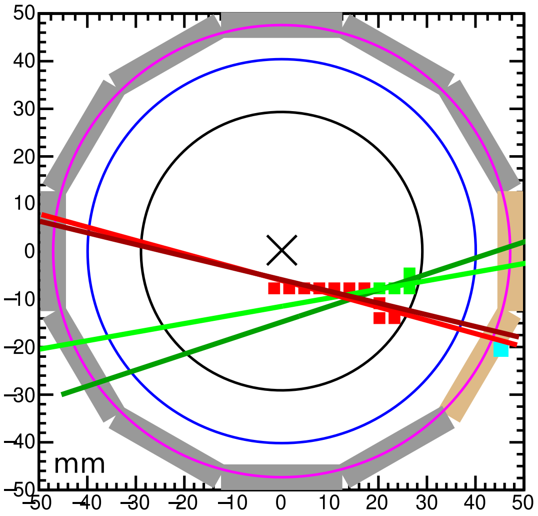

FIGURE 4.17: Illustration of the method for primary track identification Adapted from event `828/103`. For each track, two fits are calculated. One including the TOF1 (bright) and one without it (dark). The TOF1 hit point is indicated by a cyan marker. For details on the graphs elements, refer to section 4.2.1.

Parameter	Unit	Default	Optimal
`K_STOP_CENTROID_THRESH`	mm	8	2
`TWO_TRACK_MIN_LEPTON_BARS`	–	5	2
`TWO_TRACK_MIN_CHISQ`	mm^2	1	1.5
`PATH_TRAVERSIAL_DIJKSTRA_JUMP_RADIUS`	mm	9	7.5
`PATH_TRAVERSIAL_ALL_PENALTY`	–	1000	>10
`FIT_TOF1_WEIGHT`	–	3	5

TABLE 4.2: Summary of the default values used for the algorithm parameters and the optimal values found by variation.

the TOF1 value is supplied by the simulation. For experimental data, the uncertainty on its value is way bigger. Therefore, overrating its accuracy might lead to a worse analysis. The value 5 was chosen out of cautiousness.

4.4 Results

To sum up the above discussion, the set of optimal parameters found by variation is given in table 4.2. For comparison, the default values chosen during development are also listed. These could be shown to be not ideal when they are chosen naïvly.

Using the set of optimal parameters, the figures of merit explained in section 4.2.3 were calculated on the data sets listed in the same section. Their values are given in

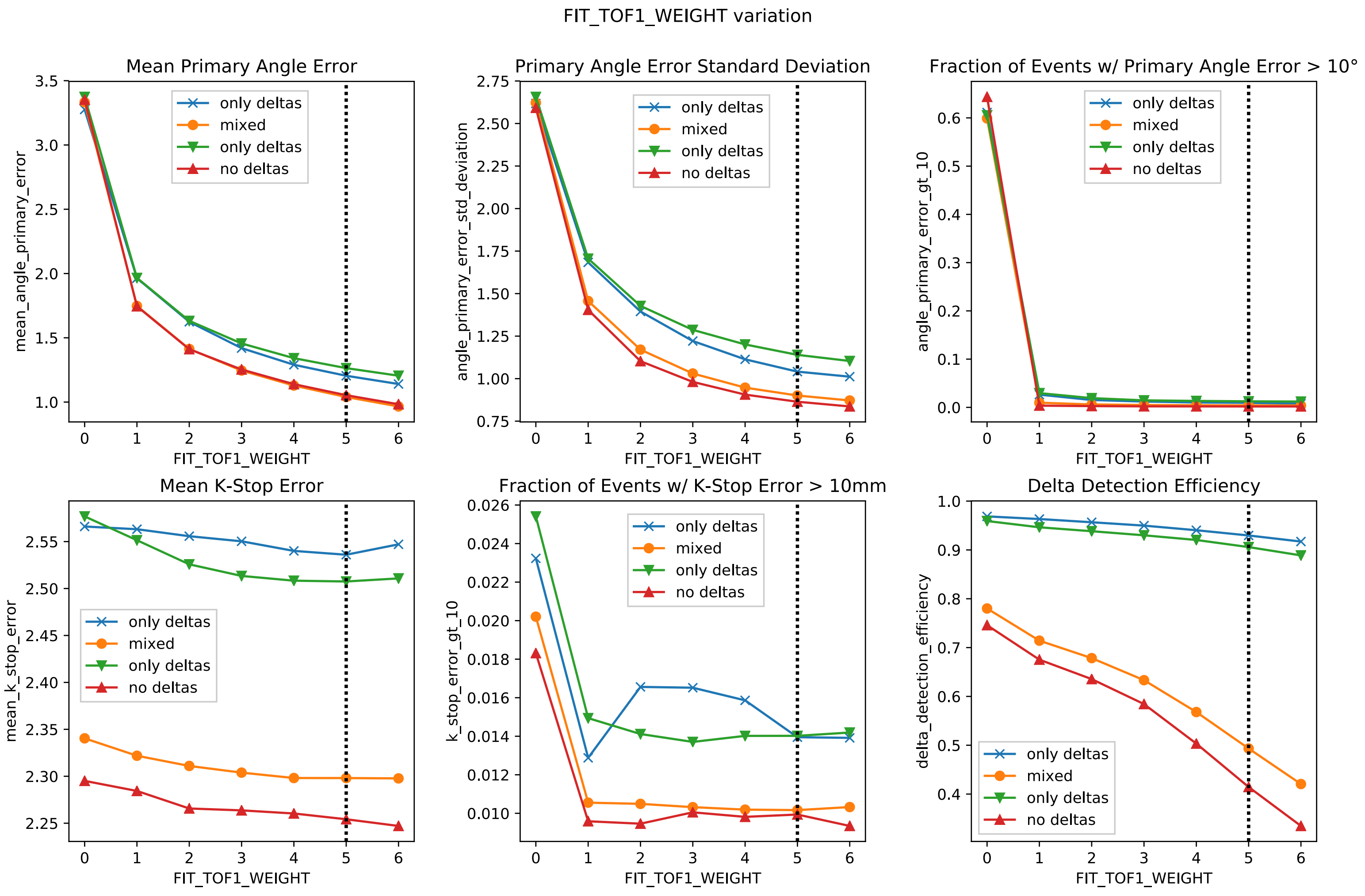

FIGURE 4.18: The influence of the variation of the parameter `FIT_TOF1_WEIGHT` on the algorithm performance. Bigger values are better. Details on graph generation in section 4.2.3.

Figure of Merit	Value	Unit
Mean Primary Angle Error	1.20	°
Primary Angle Error Standard Deviation	1.06	°
Rate of Events w/ Error > 10°	0.48	%
Delta Detection Efficiency	78.80	%
False Positive Rate	6.58	%

Table 4.3: Figures of merit for the algorithm evaluated on the set of optimal parameters. Explanation in section 4.2.3.

table 4.3. All values were averaged over the two data sets containing only knock-on electron events, except the false positive rate, which was obtained from the set only containing single track events. The meta-analysis plot summaries for all data sets with the optimized parameter set are listed in chapter 5.

The mean primary angle error is of the same order of magnitude as its standard deviation. Since both quantities seem to be minimized by the same parameter tuning, there is not much that can be done about it. In the end there will always be a finite spread in the evaluated angle, so the current values should be seen as acceptable. Overall (1.20 ± 1.06) is still a relatively small error and even if both mean and standard deviation can be driven down further by algorithm improvements, it seems unlikely that their ratio will change much.

The comparatively low detection rate could be thought of as troublesome, but in the end, the angle error matters most. While tuning the parameters, one could easily aim for a high detection efficiency, but if that drives the over all angle error up for the same data set, it doesn't make sense. That a minimized angle error results in such a low detection rate just means, that in the cases where a one track fit is wrongly attempted on a two track event, it still yields a good end result. One can therefore assume that these are events with very small delta tracks that don't affect an one track fit. Apparently it would decrease the quality of the rest of the two track fits if the parameters are adjusted to also analyze these events in a two track manner or the two track algorithm delivers worse results than a simple fit in these cases.

Chapter 5

Conclusion

In this thesis, the J-PARC/E36 experiment's goal and execution have been explained. The search for new physics and the test of lepton universality are given as a motivation for measuring the ratio $R_{\mathrm{K}}^{\mathrm{SM}}$ of electronic over muonic decay mode of the kaon system. The theoretical background necessary for understanding this project and the functionality of the detector system in use have been explained as well. A basic description of the general detector has been given, with a more in-depth focus on the segmented fiber target that plays a crucial role in the analysis. The main focus of this project has been the evaluation and optimization of one algorithm in the analysis pipeline.

To discuss the problems and solutions encountered during the work on the algorithm, it was thoroughly explained step-by-step. The applied improvements have been backed up by a numerical evaluation of parameter variation, so that the influence of different parts of the algorithm on its performance could be shown. While working on the code, different tools for data visualization and statistical analysis have been developed and their functionality laid out as well. In the end, an optimal set of parameters has been found and the resulting algorithm performance evaluated in the face of several figures of merit.

While a lot of improvements have been successfully implemented, there are still several parameters statically included in the code that could be varied and optimized. Since the algorithm has only been applied to simulation data and the analysis pipeline for the experimental results is disjunct from it, a next step would be to merge these together, so that findings from the simulation study can be transferred directly to the experimental data.

Bibliography

[1] S. Agostinelli et al. “Geant4—a simulation toolkit”. In: *Nuclear Instruments and Methods in Physics Research Section A: Accelerators, Spectrometers, Detectors and Associated Equipment* 506.3 (2003), pp. 250–303. doi: https://doi.org/10.1016/S0168-9002(03)01368-8. url: http://www.sciencedirect.com/science/article/pii/S0168900203013688 (cit. on p. 13).

[2] Q. R. Ahmad et al. “Direct Evidence for Neutrino Flavor Transformation from Neutral-Current Interactions in the Sudbury Neutrino Observatory”. In: *Phys. Rev. Lett.* 89 (1 June 2002), p. 011301. doi: 10.1103/PhysRevLett.89.011301. url: https://link.aps.org/doi/10.1103/PhysRevLett.89.011301 (cit. on p. 1).

[3] F. Ambrosino et al. “Precise measurement of $\Gamma(\mathrm{K}\to e\nu(\gamma))/\Gamma(\mathrm{K}\to\mu\nu(\gamma))$ and study of $\mathrm{K}\to \mathrm{e}\ \nu\ \gamma$”. In: *The European Physical Journal C* 64.4 (Dec. 2009), pp. 627–636. doi: 10.1140/epjc/s10052-009-1177-x. url: https://doi.org/10.1140/epjc/s10052-009-1177-x (cit. on p. 2).

[4] S. A. Bludman and J. A. Young. “Radiative Pion Decay into Electrons”. In: *Phys. Rev.* 118 (2 Apr. 1960), pp. 602–605. doi: 10.1103/PhysRev.118.602. url: https://link.aps.org/doi/10.1103/PhysRev.118.602 (cit. on p. 9).

[5] T. Bollinger, jwimberly, and M. Brown. *If helicity can suppress weak decay of $\pi^{\pm}$, doesn’t that make chiralty observer dependent?* Physics StackExchange. Mar. 20, 2013. url: https://physics.stackexchange.com/questions/57397/if-helicity-can-suppress-weak-decay-of-pi-pm-doesnt-that-make-chiralty-o/ (visited on 04/10/2018) (cit. on p. 11).

[6] R. Brun and F. Rademakers. “ROOT — An object oriented data analysis framework”. In: *Nuclear Instruments and Methods in Physics Research Section A: Accelerators, Spectrometers, Detectors and Associated Equipment* 389.1 (1997). New Computing Techniques in Physics Research V, pp. 81–86. doi: https://doi.org/10.1016/S0168-9002(97)00048-X. url: http://www.sciencedirect.com/science/article/pii/S016890029700048X (cit. on p. 25).

[7] V. Cirigliano and I. Rosell. “Two-Loop Effective Theory Analysis of π $(K) \to e\overline{\nu}_e[\gamma]$ Branching Ratios”. In: *Phys. Rev. Lett.* 99 (23 Dec. 2007), p. 231801. doi: 10.1103/PhysRevLett.99.231801. url: https://link.aps.org/doi/10.1103/PhysRevLett.99.231801 (cit. on pp. 2, 9, 10).

[8] E. W. Dijkstra. “A note on two problems in connexion with graphs”. In: *Numerische Mathematik* 1.1 (Dec. 1, 1959), pp. 269–271. doi: `10.1007/BF01386390`. url: `https://doi.org/10.1007/BF01386390` (cit. on p. 41).

[9] J. Ellis. “TikZ-Feynman: Feynman diagrams with TikZ”. In: (2016). doi: `10.1016/j.cpc.2016.08.019`. arXiv: `1601.05437` (cit. on pp. 7, 10, 12).

[10] Y. Fukuda et al. “Evidence for Oscillation of Atmospheric Neutrinos”. In: *Phys. Rev. Lett.* 81 (8 Aug. 1998), pp. 1562–1567. doi: `10.1103/PhysRevLett.81.1562`. url: `https://link.aps.org/doi/10.1103/PhysRevLett.81.1562` (cit. on p. 1).

[11] *Geant4 Physics Reference Manual.* 10.4 rev1.0. Geant4 Collaboration. Dec. 8, 2017. url: `https://geant4-userdoc.web.cern.ch/geant4-userdoc/UsersGuides/PhysicsReferenceManual/fo/PhysicsReferenceManual.pdf` (cit. on pp. 13–16).

[12] Geeks4Geeks. *Convex Hull | Set 2 (Graham Scan)*. July 24, 2013. url: `https://www.geeksforgeeks.org/convex-hull-set-2-graham-scan/` (visited on 04/07/2018) (cit. on p. 40).

[13] J. Girrbach and U. Nierste. *Gamma(K -> e nu)/Gamma(K -> mu nu) in the Minimal Supersymmetric Standard Model.* 2012. arXiv: `1202.4906` (cit. on p. 11).

[14] R. Graham. “An efficient algorith for determining the convex hull of a finite planar set”. In: *Information Processing Letters* 1.4 (1972), pp. 132–133. doi: `https://doi.org/10.1016/0020-0190(72)90045-2`. url: `http://www.sciencedirect.com/science/article/pii/0020019072900452` (cit. on p. 40).

[15] D. Griffiths. *Introduction to elementary particles.* Physics textbook. Wiley, 1987. url: `http://eu.wiley.com/WileyCDA/WileyTitle/productCd-3527406018,subjectCd-PH20.html` (cit. on pp. 1, 7).

[16] F. Hanzel and A. Martin. *Quarks and Leptons: An introductory course in modern particle phyics.* John Wiley & Sons, 1984 (cit. on p. 10).

[17] J. D. Hunter. “Matplotlib: A 2D graphics environment”. In: *Computing In Science & Engineering* 9.3 (2007), pp. 90–95. doi: `10.1109/MCSE.2007.55` (cit. on p. 26).

[18] E. Jones, T. Oliphant, P. Peterson, et al. *SciPy: Open source scientific tools for Python.* 2001–. url: `http://www.scipy.org/` (visited on 04/06/2018) (cit. on p. 26).

[19] M. Kohl. “TREK @ J-PARC: Beyond the Standard Model with Stopped K^+”. In: *Workshop on Physics with Neutral Kaon Beam at JLab (KL2016) Mini-Proceedings.* (Thomas Jefferson National Accelerator Facility, Feb. 1–3, 2016). Ed. by M. Amaryan et al. Newport News, VA, USA, 2016, pp. 191–197. arXiv: `1604.02141` (cit. on pp. 10, 17).

[20] W. R. Leo. *Techniques for Nuclear and Particle Physics Experiments.* Springer Berlin Heidelberg, 1994. doi: `10.1007/978-3-642-57920-2`. url: `https://doi.org/10.1007/978-3-642-57920-2` (cit. on p. 11).

[21] H. Lu. “Status of the E36 Experiment at J-PARC”. In: *PoS* HQL2016 (2017), p. 036 (cit. on pp. 9, 11, 17).

[22] E. H. an Maridel Lares. *What is an MPPC? Geiger-mode avalanche photodiode arrays overcome limitations of a single device, and can distinguish between multiple-photon and single-photon events.* Hamamatsu Photonics. Aug. 2008. URL: `http://www.hamamatsu.com/eu/en/community/optical_sensors/articles/intro_to_mppc/index.html` (visited on 04/10/2018) (cit. on p. 22).

[23] Y. Miyazaki et al. "Performance test of a lead-glass counter for the J-PARC E36 experiment". In: *Nuclear Instruments and Methods in Physics Research Section A: Accelerators, Spectrometers, Detectors and Associated Equipment* 779 (2015), pp. 13–17. DOI: `https://doi.org/10.1016/j.nima.2015.01.044`. URL: `http://www.sciencedirect.com/science/article/pii/S0168900215000753` (cit. on p. 20).

[24] D. E. Neville. "Radiative Modes of K-Meson Leptonic Decay". In: *Phys. Rev.* 124 (6 Dec. 1961), pp. 2037–2046. DOI: `10.1103/PhysRev.124.2037`. URL: `https://link.aps.org/doi/10.1103/PhysRev.124.2037` (cit. on pp. 9, 10).

[25] J. C. Pati and A. Salam. "Lepton number as the fourth "color"". In: *Phys. Rev. D* 10 (1 July 1974), pp. 275–289. DOI: `10.1103/PhysRevD.10.275`. URL: `https://link.aps.org/doi/10.1103/PhysRevD.10.275` (cit. on p. 1).

[26] C. Patrignani et al., Particle Data Group. "Review of Particle Physics". In: *Chin. Phys.* C40.10 (2016), p. 100001. DOI: `10.1088/1674-1137/40/10/100001` (cit. on pp. 1, 2, 6, 9, 11, 15).

[27] M. Peskin and D. Schroeder. *An Introduction to Quantum Field Theory.* Advanced book classics. Addison-Wesley Publishing Company, 1995 (cit. on pp. 5, 7, 9, 15).

[28] *Precision Measurement of the Ratio of the Charged Kaon Leptonic Decay Rates.* The NA62 collaboration, 2012. eprint: `arXiv:1212.4012` (cit. on p. 2).

[29] C. Rangacharyulu et al. *J-PARC Experimental Proposal Measurement of $\Gamma(K^+ \to e^+\nu)/\Gamma(K^+ \to \mu^+\nu$ and Search for heavy sterile neutrinos using the TREK detector system.* Proposal. J-PARC TREK Collaboration, June 2010. URL: `http://j-parc.jp/researcher/Hadron/en/pac_1007/pdf/KEK_J-PARC-PAC2010-04.pdf` (cit. on pp. 2, 6, 8, 9, 11–13, 17, 18).

[30] S. M. Seltzer and M. J. Berger. "Bremsstrahlung spectra from electron interactions with screened atomic nuclei and orbital electrons". In: *Nuclear Instruments and Methods in Physics Research Section B: Beam Interactions with Materials and Atoms* 12.1 (1985), pp. 95–134. DOI: `https://doi.org/10.1016/0168-583X(85)90707-4`. URL: `http://www.sciencedirect.com/science/article/pii/0168583X85907074` (cit. on p. 16).

[31] S. Shimizu. "E36 progress report. Measurement of $\Gamma(K^+ \to e^+\nu)/\Gamma(K^+ \to \mu^+\nu$". In: 16th PAC meeting. Jan. 9, 2013. URL: `http://nuclpart.kek.jp/pac/1301/pdf/PAC1301-e36sshimizu2-open.pdf` (cit. on p. 21).

[32] S. Strauch. "Searches for New Physics with the TREK Detector". In: *PoS* KAON13 (2013), p. 014 (cit. on p. 9).

[33] *Systematic Error Analysis of the Measurement of* $\Gamma(K^+ \to e^+\nu)/\Gamma(K^+ \to \mu^+\nu$. *Addendum II to Proposal P36*. Proposal. J-PARC TREK Collaboration, Jan. 2012. URL: `http://trek.kek.jp/e36/reports/kl2add2_submitted.pdf` (cit. on pp. 17, 20, 21).

[34] S. Weinzierl. *Introduction to Monte Carlo methods*. 2000. eprint: `arXiv:hep-ph/0006269` (cit. on p. 13).

[35] E. W. Weisstein. *Chi-Squared Distribution*. From MathWorld–A Wolfram Web Resource. 2002. URL: `http://mathworld.wolfram.com/Chi-SquaredDistribution.html` (visited on 04/16/2018) (cit. on p. 45).

Acknowledgements

The experiment and its evalulation is a joint efford of an international collaboration. These collaborators are

> **Canada:** University of Saskatchewan, University of British Columbia, TRIUMF, Universite de Montreal **USA:** University of South Carolina, Iowa State University, Hampton University & Jefferson Laboratory **Russia:** Institute for Nuclear Research (INR) **Japan:** Osaka University, Tohoku University, Tokyo Institute of Technology, Chiba University, University of Tokyo, Rikkyo University, High Energy Accel. Research Organization (KEK) **Korea:** Kyungpook National University, Korea University **Vietnam:** University of Natural Sciences

Support for the research comes from

> **Canada:** NSERC, NRC **Japan:** KAKEN-HI Grants-in-Aid for Scientific Research **USA:** DOE, NSF **Russia:** Ministry of Science and Technology

In particular, I want to thank my supervisors Mike Hasinoff (UBC) and Sebastien Bianchin (TRIUMF), for their patience and helpful advice. Their guidance and support has been essential in the research and preparation of the thesis. I also would like to Jun Imazato (KEK), who generated the simulation data files, often very quickly upon my request, and for clarifications concerning their implementation.

In general, Robert Kiefl and Javed Iqbal from the UBC Department of Physics deserve to be mentioned here for organizing everything necessary for me to be able to take part in this project.

As always, Yannik Zimmermann shall be noted for his valuable input during our physics discussions. I also owe special thanks to Chloe He, who proof read this document under extreme circumstances and helped me improve my English significantly.

In the end, I'd like to thank the Co-op students at TRIUMF for being good company during the lunch breaks.

Meta-Analysis with Optimized Parameters

run number	828
number of events	1573
delta detection efficiency	80.10%
mean primary angle error	1.16°
primary angle error std deviation	1.00°
mean difference one/two-track fit	2.71°
mean K-stop error	2.44mm
fraction events k_stop_error > 10	0.57%
fraction events angle_primary_error > 10	1.02%
events with missing tracks (kaon/lepton)	6.42%

TWO_TRACK_MIN_CHISQ	1.5
TWO_TRACK_MIN_LEPTON_BARS	2.0
FIT_TOF1_WEIGHT	5.0
K_STOP_CENTROID_THRESH	2.0
PATH_TRAVERSIAL_USE_ALL	0.0
PATH_TRAVERSIAL_DIJKSTRA_JUMP_RADIUS	7.5
PATH_TRAVERSIAL_ALL_PENALTY	1000.0

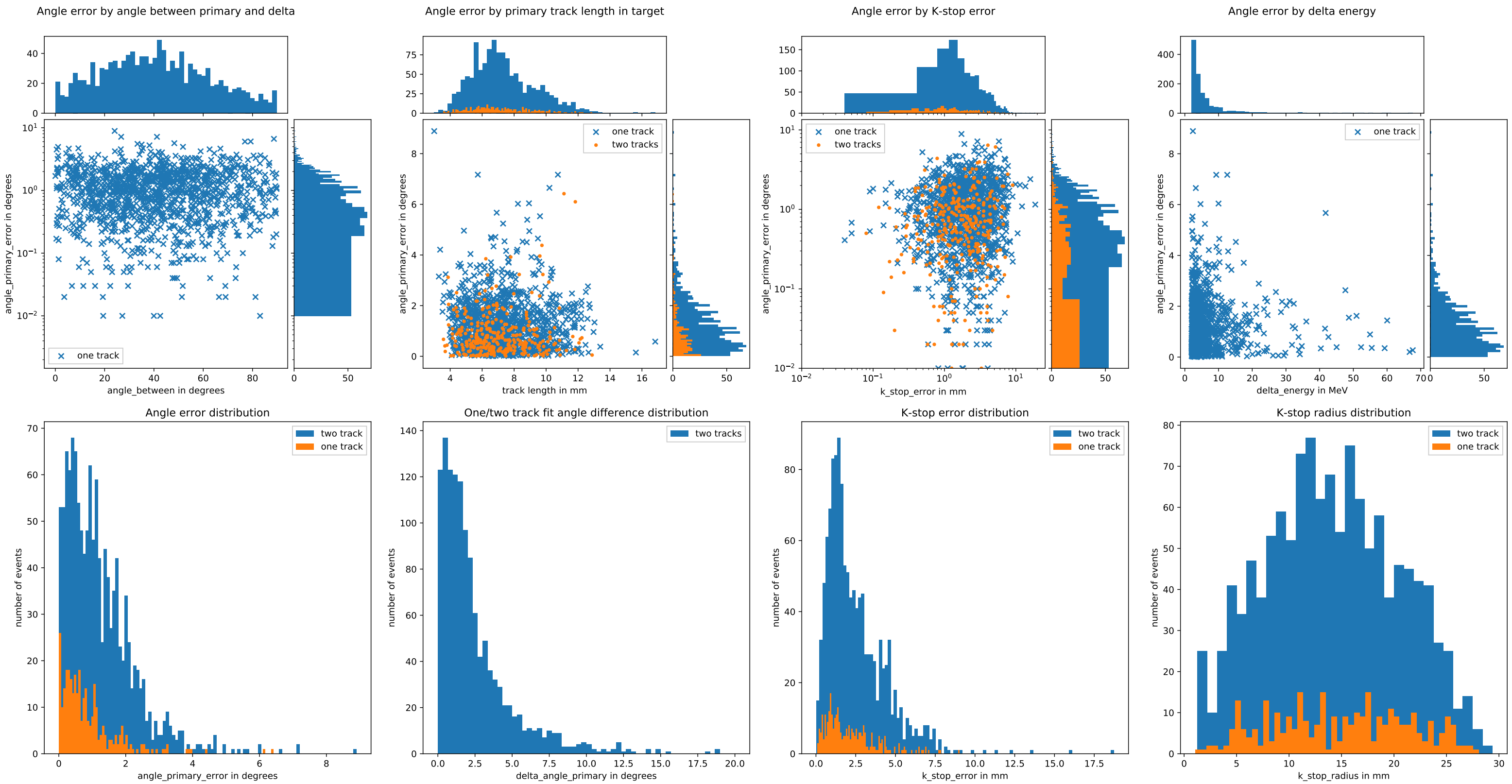

FIGURE A.1: Meta-analysis of data set 828 with optimal parameters. Details on graph generation in section 4.2.2.

run number	2141
number of events	38041
delta detection efficiency	15.89%
mean primary angle error	0.92°
primary angle error std deviation	0.86°
mean difference one/two-track fit	2.40°
mean K-stop error	2.27mm
fraction events k_stop_error > 10	0.36%
fraction events angle_primary_error > 10	0.41%
events with missing tracks (kaon/lepton)	20.08%

TWO_TRACK_MIN_CHISQ	1.5
TWO_TRACK_MIN_LEPTON_BARS	2.0
FIT_TOF1_WEIGHT	5.0
K_STOP_CENTROID_THRESH	2.0
PATH_TRAVERSIAL_USE_ALL	0.0
PATH_TRAVERSIAL_DIJKSTRA_JUMP_RADIUS	7.5
PATH_TRAVERSIAL_ALL_PENALTY	1000.0

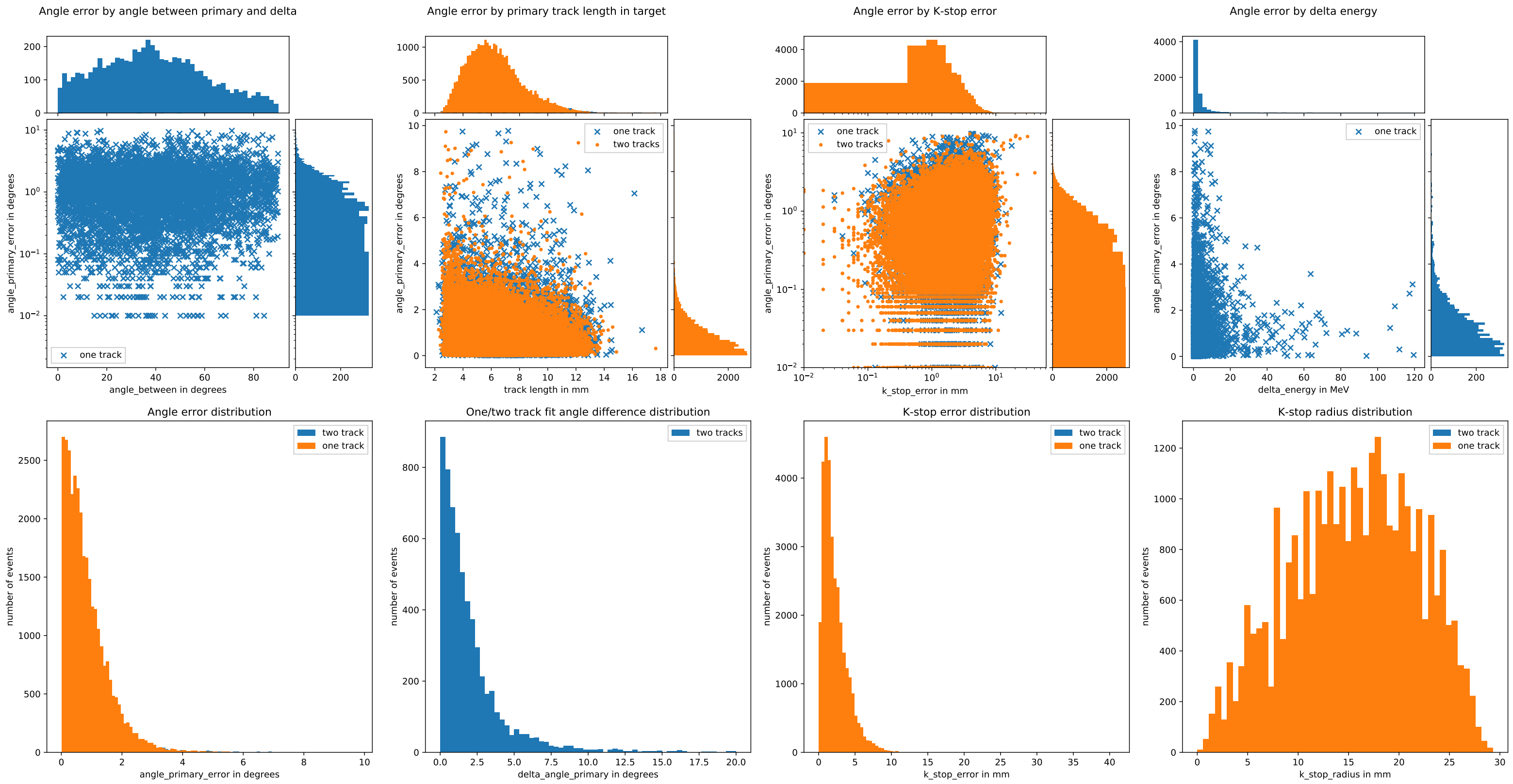

Figure A.2: Meta-analysis of data set 214-1 with optimal parameters. Details on graph generation in section 4.2.2.

run number	2161
number of events	5977
delta detection efficiency	77.50%
mean primary angle error	1.23°
primary angle error std deviation	1.11°
mean difference one/two-track fit	2.77°
mean K-stop error	2.42mm
fraction events k_stop_error > 10	0.38%
fraction events angle_primary_error > 10	1.46%
events with missing tracks (kaon/lepton)	6.12%

TWO_TRACK_MIN_CHISQ	1.5
TWO_TRACK_MIN_LEPTON_BARS	2.0
FIT_TOF1_WEIGHT	5.0
K_STOP_CENTROID_THRESH	2.0
PATH_TRAVERSIAL_USE_ALL	0.0
PATH_TRAVERSIAL_DIJKSTRA_JUMP_RADIUS	7.5
PATH_TRAVERSIAL_ALL_PENALTY	1000.0

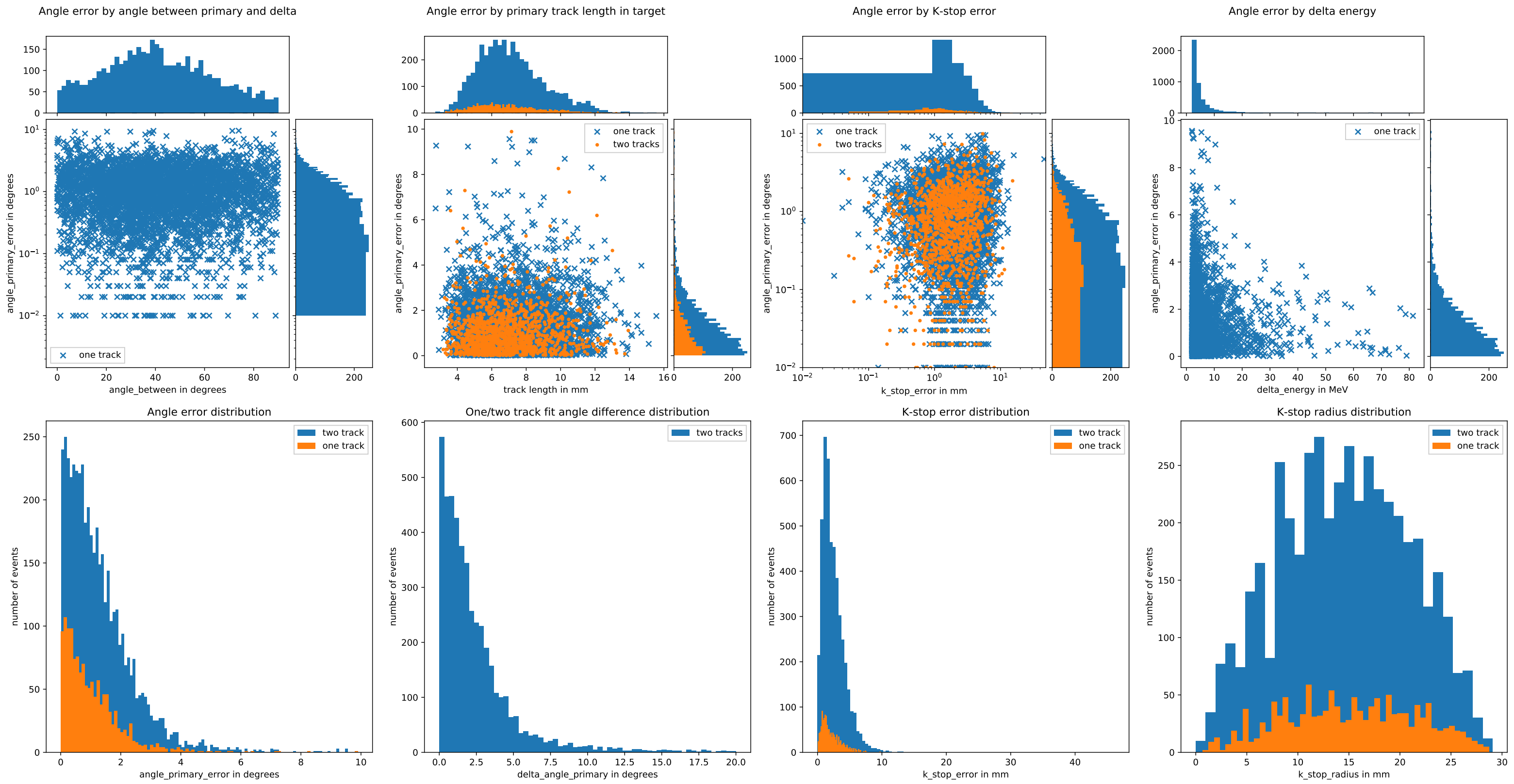

Figure A.3: Meta-analysis of data set `216-1` with optimal parameters. Details on graph generation in section 4.2.2.

run number	3212
number of events	8354
delta detection efficiency	6.58%
mean primary angle error	0.94°
primary angle error std deviation	0.82°
mean difference one/two-track fit	2.40°
mean K-stop error	2.23mm
fraction events k_stop_error > 10	0.31%
fraction events angle_primary_error > 10	0.14%
events with missing tracks (kaon/lepton)	23.15%

TWO_TRACK_MIN_CHISQ	1.5
TWO_TRACK_MIN_LEPTON_BARS	2.0
FIT_TOF1_WEIGHT	5.0
K_STOP_CENTROID_THRESH	2.0
PATH_TRAVERSIAL_USE_ALL	0.0
PATH_TRAVERSIAL_DIJKSTRA_JUMP_RADIUS	7.5
PATH_TRAVERSIAL_ALL_PENALTY	1000.0

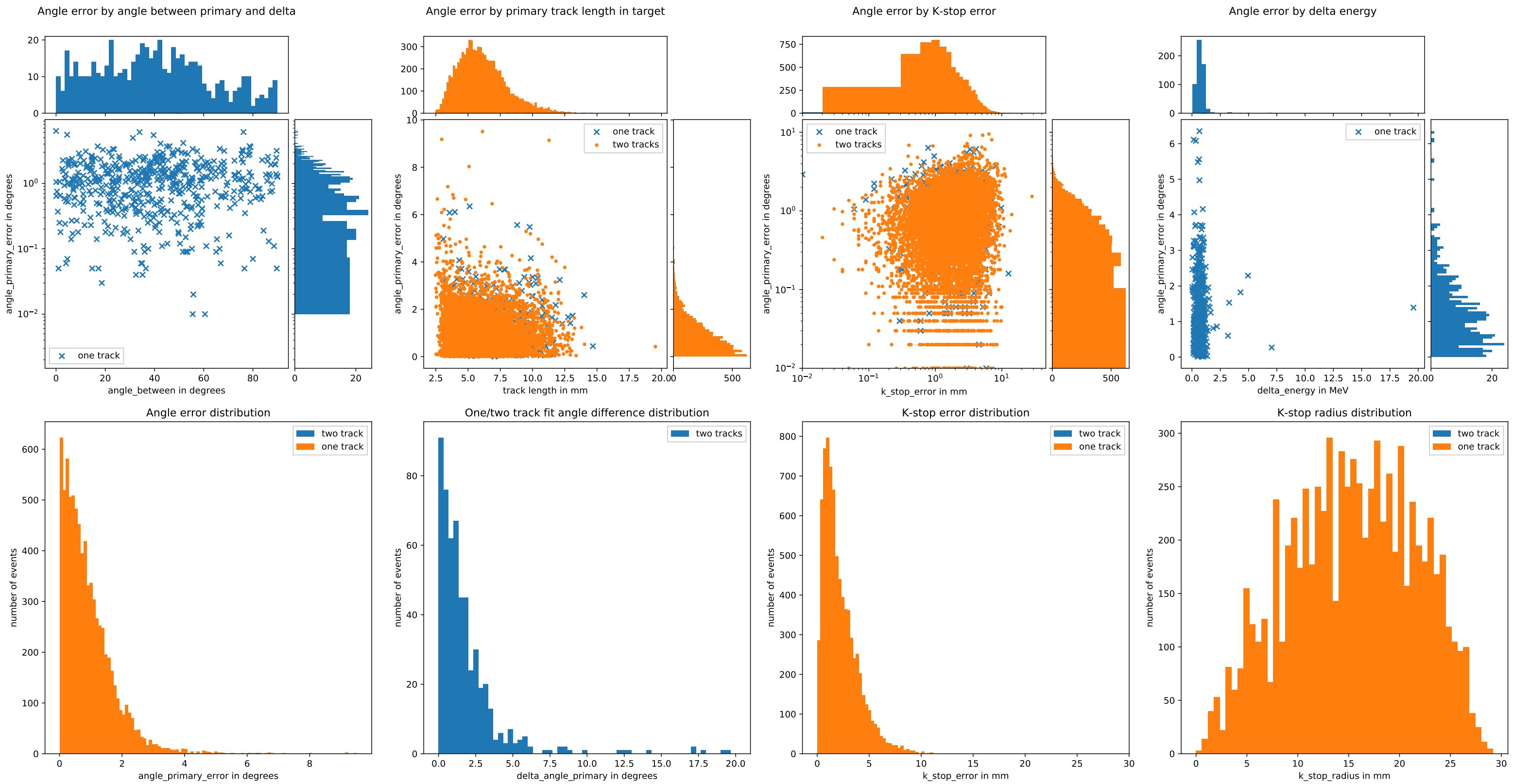

FIGURE A.4: Meta-analysis of data set 321-2 with optimal parameters. Details on graph generation in section 4.2.2.